Atomistic dynamics of crack propagation in complex metallic alloys

Von der Fakultät Mathematik und Physik
der Universität Stuttgart
zur Erlangung der Würde eines Doktors der
Naturwissenschaften (Dr. rer. nat.) genehmigte Abhandlung

Vorgelegt von
Frohmut Matthias Rösch
aus Heilbronn

Hauptberichter: Prof. Dr. Hans-Rainer Trebin
Mitberichter: Prof. Dr. Siegfried Schmauder

Tag der mündlichen Prüfung: 21. Juli 2008

Institut für Theoretische und Angewandte Physik
Universität Stuttgart

2008

Für meine Eltern

Parts of this work have already been published:

[92] F. Rösch, C. Rudhart, J. Roth, H.-R. Trebin, and P. Gumbsch, Dynamic fracture of icosahedral model quasicrystals: A molecular dynamics study, *Phys. Rev. B* **72** (2005) 014128.

[94] F. Rösch, H.-R. Trebin, and P. Gumbsch, Fracture of complex metallic alloys: An atomistic study of model systems, *Phil. Mag.* **86** (2006) 1015–1020.

[95] F. Rösch, H.-R. Trebin, and P. Gumbsch, Interatomic potentials and the simulation of fracture: C15 $NbCr_2$, *Int. J. Fracture* **139** (2006) 517–526.

Contents

Zusammenfassung **7**

Introduction **11**

1 Complex metallic alloys **13**
- 1.1 Quasicrystals 13
  - 1.1.1 Icosahedral binary model 13
- 1.2 Friauf-Laves phases 14

2 Fracture mechanics **19**
- 2.1 Linear elastic theory 19
- 2.2 The Griffith criterion 20
- 2.3 Propagating cracks 21
- 2.4 Effects of discrete structures 21
- 2.5 Brittleness and ductility 22

3 Numerical methods **25**
- 3.1 Ab-initio calculations 25
  - 3.1.1 Density functional theory 26
  - 3.1.2 Plane-wave basis 27
  - 3.1.3 Valence and core electrons 28
- 3.2 Molecular dynamics simulations 29
  - 3.2.1 Effective potentials 29
  - 3.2.2 Boundaries 31
  - 3.2.3 Statistical mechanics 31
  - 3.2.4 Ensembles and relaxators 32
  - 3.2.5 Fracture studies 33
    - Sample preparation 34
    - Visualization 35
    - Abbreviations 36

4 Results and discussion **39**
- 4.1 Model systems 39
  - 4.1.1 Model quasicrystal 41
  - 4.1.2 Model Friauf-Laves phase 46
- 4.2 C15 $NbCr_2$ 49
  - 4.2.1 Effective potentials 50
  - 4.2.2 Validation of the potentials 51

Lattice constant 52
Elastic properties 52
Melting temperature 54
Free surfaces 55
4.2.3 Fracture simulations 62
Orientations 63
Velocities 63
Fracture surfaces 68
Shifted seed cracks 80
Energy considerations 80
Atomistic aspects 84

Summary **87**

Appendix **89**

List of Figures and Tables **93**

Lebenslauf **107**

Danksagung **109**

Zusammenfassung

Der Bruch fester Materie geschieht durch die Ausbreitung von Rissen und ist uns aus dem Alltag vertraut. Ein zerbrochener Teller oder ein zerschlagenes Glas ist lästig. Versagt dagegen der Rumpf eines Schiffes oder der eines Flugzeuges, kann dies Menschen das Leben kosten. Gleichwohl wurde erst in den letzten Jahren Einblick in die grundlegenden Mechanismen gewonnen, die zum Versagen von Festkörpern durch Rissbildung führen. Ein Grund hierfür ist, dass Bruch ein Multi-Skalen-Phänomen darstellt. Eine makroskopisch von außen angelegte Spannung wird an der Rissspitze verstärkt. Daraufhin werden atomare Bindungen gebrochen. Um Bruchmechanismen makroskopischer Bauteile zu verstehen, wird somit die Kenntnis von Prozessen auf atomarer Ebene benötigt. Diese sind durch heutige experimentelle Techniken kaum zugänglich, insbesondere dann nicht, wenn dynamische Aspekte im Mittelpunkt des Interesses stehen. Solche Prozesse sind auch in der klassischen Elastizitätstheorie des Bruchs nicht berücksichtigt. Computersimulationen haben sich als nützliches Hilfsmittel zur Untersuchung atomarer Vorgänge erwiesen. In Molekulardynamik-Simulationen werden die Bahnen der Atome durch Integration der Newton'schen Bewegungsgleichungen berechnet. Numerische Experimente mit einfachen Kristallstrukturen und Modellwechselwirkungen lassen Effekte erkennen, für die der diskrete Aufbau der Materie verantwortlich ist. Kontinuumstheorien sind daher nicht geeignet, die erwähnten Phänomene zu erklären. Die Vorgänge in komplexeren Festkörpern sind bis heute noch nicht vollständig verstanden. Um einen Einblick in die grundlegenden Mechanismen zu erhalten, wird in der vorliegende Arbeit das Bruchverhalten komplexer metallischer Verbindungen bei tiefen Temperaturen mit Hilfe der Molekulardynamik untersucht.

Komplexe intermetallische Verbindungen weisen große Einheitszellen auf. Oft existieren Gruppierungen von Atomen, sogenannte Cluster, die als Bausteine der Struktur angesehen werden können. Häufig sind interessante physikalischen Eigenschaften kombiniert, wie z.B. ein hoher Schmelzpunkt und eine geringe Dichte. Allerdings sind die Einsatzmöglichkeiten der Materialien meist durch eine extreme Sprödigkeit bei Raumtemperatur und bei tiefen Temperaturen begrenzt. Zwei strukturelle Extremfälle wurden ausgewählt, um zum Einfluss der Komplexität auf das Bruchverhalten untersucht zu werden: ein Modell-Quasikristall und eine C15-Friauf-Laves-Phase. Quasikristalle besitzen eine

Translationsordnung langer Reichweite, ohne periodisch zu sein. Eine wohldefinierte atomare Ebenenstruktur führt dazu, dass Beugungsbilder scharfe Braggpeaks zeigen. Cluster mit Ikosaedersymmetrie bestimmen die Struktur. Bausteine des Quasikristalles (jedoch nicht die Cluster) finden sich in der C15-Phase wieder. Die kubische Einheitszelle ist mit 24 Atomen besetzt. Die Friauf-Laves-Phasen sind der wichtigste Vertreter der topologisch dicht gepackten intermetallischen Verbindungen.

Beim Dehnen einer Probe wird elastische Energie im System gespeichert. Läuft ein Riss durch einen gedehnten spröden Festkörper, werden freie Oberflächen erzeugt. Daher sollte ein Riss sich ausbreiten können, falls die elastische Energie zur Erzeugung der Bruchoberflächen genügt. Diese Folgerung wird oft Griffith-Kriterium genannt. Solch ein globales thermodynamisches Bild des Bruchs berücksichtigt nicht den Einfluss des diskreten atomaren Aufbaus der Materie. Die Stärke und Anordnung lokaler Bindungen könnte jedoch das Bruchverhalten beeinflussen. Auswirkungen jener Art werden in der vorliegenden Schrift mit Hilfe atomistischer numerischer Bruchsimulationen untersucht.

Zunächst werden Modellwechselwirkungen angesetzt (siehe Kapitel 4.1). Der Quasikristall zeigt ein sprödes Bruchverhalten unabhängig von der Probenorientierung. Risse breiten sich nur für Lasten aus, die über den Vorhersagen des Griffith-Kriteriums liegen. Ein solches Verhalten ist bereits aus Simulationen einfacherer Systeme bekannt. Aufgrund des Atomgitters müssen lokal Bindungen gebrochen werden. Das führt dazu, dass ein Riss innerhalb eines Belastungsbereiches vom Gitter stabilisiert wird und sich nicht ausbreitet oder schließt. Durch den *lattice-trapping* genannten Effekt steht bei einer angelegten Last, die Rissausbreitung ermöglicht, von Beginn an mehr Energie zur Verfügung als zur Generierung glatter Oberflächen notwendig wäre. Daher müssen Bruchoberflächen nicht notwendigerweise die kleinste Oberflächenenergie oder die geringste Rauigkeit aufweisen. Die Bruchoberflächen des Modellquasikristalles sind auf Clusterskala rau. Auswertungen der Simulationen zeigen, dass die Anzahl und die Verteilung der Cluster das Bruchverhalten beeinflussen. Risse wählen Pfade, die weniger Cluster durchtrennen aber insgesamt mehr Energie benötigen als glatte, ebene Schnitte. Strukturen in den Höhenprofilen der Bruchoberflächen und unterschiedliche Ausbreitungsgeschwindigkeiten der Risse können durch die Anordnung der

Cluster erklärt werden. Somit sind ein globales Energiekriterium und eine Kontinuumsbeschreibung nicht ausreichend, um das Bruchverhalten komplexer Systeme zu erklären. Ein weiterer interessanter Aspekt tritt bei der Rauigkeit von Quasikristall-Bruchflächen auf. Trotz des eindeutigen Einflusses der Cluster zeigen sich keine Auffälligkeiten in der Selbstähnlichkeit der Höhen-Höhen-Korrelationsfunktion verglichen mit anderen Substanzen. Die numerischen Simulationen hierzu sind in Kapitel 4.1.1 und im Anhang geschildert. Aufgrund der strukturellen Ähnlichkeit wird das Bruchverhalten einer C15-Friauf-Laves-Phase mit den Modellwechselwirkungen des Quasikristalles untersucht. Das Fehlen der Cluster im C15-Modellkristall äußert sich in einer nur auf atomarer Skala rauen Bruchoberfläche. Die numerischen Experimente zeigen somit, dass die grundlegenden Bausteine der Strukturen – Atome bzw. Cluster – auch die Rissausbreitung beeinflussen. Somit erlauben die Modellsysteme eine qualitative Aussage über den Einfluss der Struktur auf das Bruchverhalten.

Der Hauptteil der vorliegenden Arbeit beschäftigt sich mit der Simulation der Friauf-Laves-Phase $NbCr_2$ (siehe Kapitel 4.2), welche dieselbe C15-Struktur wie der Modellkristall besitzt. Für die interatomaren Wechselwirkungen werden Potenziale benötigt, die quantitativ die physikalischen Eigenschaften der realen Verbindung wiedergeben. Für einfache Metalle existieren diverse Wechselwirkungen, die experimentell gemessene Werte oder quantenmechanisch berechnete Gleichgewichtseigenschaften reproduzieren. Meist werden hierzu analytisch angesetzte Formulierungen benutzt, deren Parameter dann an einige wenige materialspezifische Größen angepasst sind. Für komplexe intermetallische Verbindungen sind nahezu keine Potenziale erhältlich. Eine Methode, letztere zu erzeugen, ist das sogenannte *force-matching*-Verfahren. Hierbei werden quantenmechanisch berechnete Kräfte zur Anpassung der in der Molekulardynamik erforderlichen Wechselwirkungen benutzt. Als Potenzialmodell wurde die *embedded atom method* ausgewählt. Neben reinen Paartermen enthält das Modell auf einfache Weise Mehrkörperwechselwirkungen. Die entsprechenden Potenzialfunktionen wurden mit Spline-Kurven so angepasst, dass die ab-initio Referenzwerte durch die effektiven Wechselwirkungen gut wiedergegeben werden. Tests zeigen, dass die so erzeugten Potenziale für $NbCr_2$ auch für Materialeigenschaften zufriedenstellende Ergebnisse liefern, die nicht direkt in die Potenzialoptimierung eingegangen sind.

Mit Hilfe der Wechselwirkungen wurde die Rissausbreitung in $NbCr_2$ in Abhängigkeit von der Orientierung und der angelegten Last untersucht. Wie in den Modellsystemen breiten sich Risse nur für Lasten oberhalb des Griffith-Kriteriums aus. Das *lattice-trapping* weist eine Abhängigkeit von der Probenorientierung auf. Alle Proben zeigen ein sprödes Bruchverhalten. Die Rauigkeit und die Oberflächenenergien der Bruchoberflächen sowie der Pfad und die Geschwindigkeit des Risses hängen hierbei nicht nur von der vorgegebenen Bruchebene ab, sondern auch von der Ausbreitungsrichtung in der Ebene. Dieses Ergebnis verdeutlicht den Einfluss der atomistischen Struktur der Materie auf das Bruchverhalten. Die Anzahl, Stärke und Orientierung der interatomaren Bindungen entlang der Rissfront bestimmen, ob und wie sich ein Riss ausbreitet.

Zusammenfassend wurde gezeigt, dass es möglich ist, qualitative und quantitative Informationen zur Rissausbreitung in komplexen intermetallischen Verbindungen mit Hilfe numerischer Experimente zu gewinnen. Detaillierte Untersuchungen der Simulationen zeigen, dass Prozesse auf atomarer Skala für das Bruchverhalten verantwortlich sind.

Introduction

The failure of solid matter is familiar to us from everyday life. A broken dish or a shattered glass is annoying. The breakage of a ship or an airplane hull, however, can cost human lives. Nevertheless, insight into the fundamental mechanisms leading to fracture has been gained only within the last couple of years. One reason for this is that fracture is a multi-scale phenomenon. A macroscopic external strain is directed to the crack tip, where it breaks atomic bonds. Thus, to understand fracture mechanisms in macroscopic devices, one also has to know the processes on the atomic scale. These are hardly accessible by experiments, in particular when dynamic aspects are the center of interest. They are also not included in the classical elastic theory of fracture. Computer simulations have proven to be a useful tool to examine fracture processes on an atomic level. In molecular dynamics simulations the trajectories of the atoms are calculated by integration of Newton‘s equations of motion. Numerical experiments with simple crystal structures and model interactions reveal phenomena that are related to the discrete nature of matter and therefore cannot be explained by continuum theories. In more complex systems the mechanisms are not yet clear.

In the current work two extreme cases of complex metallic alloys are investigated. The model quasicrystal is built-up mainly from atomic clusters. Due to the aperiodic long-range order, no unit cell exists. A major building block of the quasicrystal can also be used to obtain a periodic Friauf-Laves compound. The Friauf-Laves phases are topologically close-packed binary structures and form a huge class of intermetallic compounds. Among them are many candidates for high-temperature use. However, their brittleness at low and ambient temperature limits applications. Molecular dynamics simulations are performed to examine this brittle behavior at low temperature. First, model potentials are applied to qualitatively probe the influence of the underlying structure on crack propagation. In a second step, a specific Friauf-Laves compound is chosen. Interatomic potentials are constructed, which reproduce quantities obtained by quantum-mechanical calculations. Systematic fracture simulations then are performed.

A short introduction to the structure of the model quasicrystal and the Friauf-Laves phases is given in chapter 1. Chapter 2 contains fundamental findings of fracture mechanics, which are important for the simulations. The applied numerical methods are presented in detail in chapter 3. The results of the simulations are summarized and discussed in chapter 4.

Chapter 1

Complex metallic alloys

Complex metallic alloys (CMAs) [109][1] are intermetallic compounds with large unit cells containing from tens up to thousands of atoms. Often, distinct local arrangements of atoms, clusters, can be viewed as building units. CMAs frequently combine interesting properties such as high melting point, high-temperature strength, and low density. However, possible applications are often limited by extreme brittleness at low or ambient temperature. To enlighten the role of structural complexity in fracture, we investigate two extreme cases of CMAs: An icosahedral model quasicrystal and a C15 Friauf-Laves phase.

1.1 Quasicrystals

Quasicrystals (see, e.g., [27, 57, 60, 73, 101, 108]) are intermetallic compounds with long-range quasi-periodic translational order. They possess well-defined atomic planes and hence diffract electromagnetic and matter waves into sharp Bragg spots. But they also display atomic clusters as basic building blocks [32, 48], whose arrangement in space is compatible with the planar structure. These clusters consist for example of several shells of icosahedral symmetry (Bergman-, Mackay-, pseudo-Mackay-clusters). Or they form polytopes, e.g. decagonal prisms, which like the unit cells of periodic crystals fill space, although with large overlaps (“quasi-unit-cell picture”) [103]. Janot and others [58, 59, 61] have postulated that a self-similar hierarchical assembly of the clusters is responsible for the stability of quasicrystals and for many physical properties, like the low electric conductivity.

1.1.1 Icosahedral binary model

The three-dimensional model quasicrystal used in our numerical experiments has been proposed by Henley and Elser [49] as a structure model for the icosahedral phase of (Al,Zn)Mg. This is the simplest possible model quasicrystal that is stabilized by pair potentials. Furthermore it allows Burgers circuit analysis and is a prototype of Bergman-type quasicrystals. As we do not distinguish between Al and Zn atoms, we term the decoration icosahedral binary model. It can be obtained by decorating the structure elements of the three-dimensional Penrose tiling, the oblate and the prolate rhombohedra (see figure 1.1, top). Al and Zn atoms (X atoms) are placed on the vertices and the midpoints of the edges of the rhombohedra. Two Mg atoms (Y atoms) divide the long body diagonal of each prolate rhombohedron in ratios τ:1:τ, where τ is the golden mean. Two prolate and two oblate rhombohedra with a common vertex form a rhombic dodecahedron[2]. To obtain the icosahedral binary model, in these dodecahedra the atom at the common vertex is removed and the four neighboring X atoms are transformed into Y atoms. Finally, these atoms are shifted to the common vertex to divide the edges of the corresponding rhombohedra in a ratio of 1:τ. Figure 1.1 (bottom left) shows the final decoration of the dodecahedra, in which the Y atoms form hexagonal bipyramides. This modification increases the number of Bergman-type clusters (see figure 1.1, bottom right) inherent in the structure, leads to a higher stability with the potentials used, and takes better into account the experimentally observed stoichiometry of the quasicrystal. The Bergman-type clusters may also be interpreted as building units of the quasicrystal and are the main feature of the structure apart from the plane structure.

---

[1] CMAs are sometimes also called “structurally complex alloy phases”.

1.2 Friauf-Laves phases

The Friauf-Laves phases are often only named Laves phases, though they were discovered by Friauf [38, 39] but extensively studied by Laves [71, 72]. They are formed by elements whose atomic diameters are approximately in the ratio of 1.2:1. Hence they often are termed size components. The group of Friauf-Laves phases is the largest subset of topologically close-packed intermetallic compounds [114]. There are three main structural variants corresponding to $MgZn_2$ (C14), $MgCu_2$ (C15), and $MgNi_2$ (C36). They can be described by different stackings

---

[2] In rings of oblate rhombohedra the number of clusters is maximized. No overlapping rhombic dodecahedra are generated. Remaining oblate rhombohedra stay unchanged.

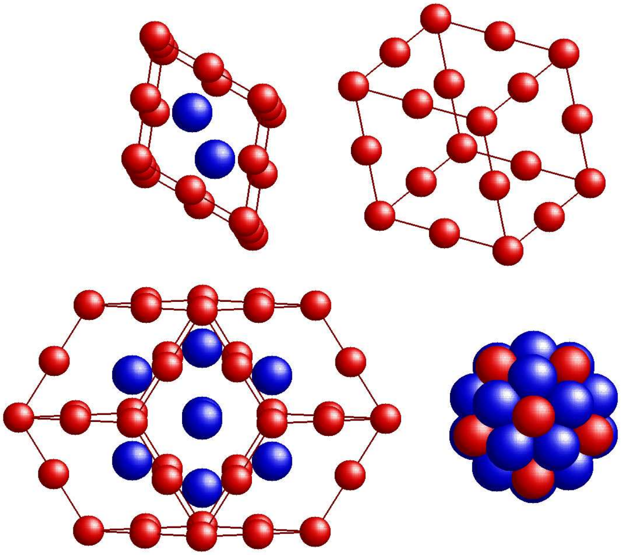

Figure 1.1: Tiles of the icosahedral binary model decorated with two types of atoms and the Bergman-type cluster. *Top:* prolate rhombohedron (left) and oblate rhombohedron (right). *Bottom:* rhombic dodecahedron (left) and the 45 atoms building the Bergman-type cluster (right) inherent in the model quasicrystal. Small red and large blue spheres denote X and Y atoms respectively.

of layers (see, e.g. [47, 76]) similarly to the relationship between face-centered cubic and hexagonal close-packed structures. In the Friauf-Laves phases YX_2 two kinds of layers are present formed by a kagome and a triangular net. The stacking sequences can be described as follows:

$$\text{C14, hexagonal:}\quad \alpha\,A\,\alpha \quad c \quad \beta\,B\,\beta \quad c\ldots \tag{1.1}$$

$$\text{C15, cubic:}\quad \alpha\,A\,\alpha \quad c \quad \beta\,B\,\beta \quad a \quad \gamma\,C\,\gamma \quad b\ldots \tag{1.2}$$

$$\text{C36, dihexagonal:}\quad \alpha\,A\,\alpha \quad c \quad \beta\,B\,\beta \quad c \quad \alpha\,A\,\alpha \quad b \quad \gamma\,C\,\gamma \quad b\ldots \tag{1.3}$$

Here upper case letters represent kagome and lower case letters triangular nets (see figure 1.2). Layers of big Y atoms are represented by Greek and those of small X atoms by Latin letters. The letter itself indicates the in-plane position of the atoms in the layer. In the C15 structure the Y atoms form a diamond lattice, whereas the X atoms build a tetrahedral network (see figure 1.3). The Friauf-Laves phases can also be formed by slightly deformed[3] prolate rhombohedra [49, 115] but not in a uniquely defined way. Because of the already quite complex structure new deformation modes like synchro-shearing (see, e.g., [20]) might emerge.

---

[3] The angles formed by two edges at the tip of the rhombohedron (see upper left corner of figure 1.1) are decreased from 63.43° to 60°. The corresponding tips are formed by the tetrahedra in figure 1.3.

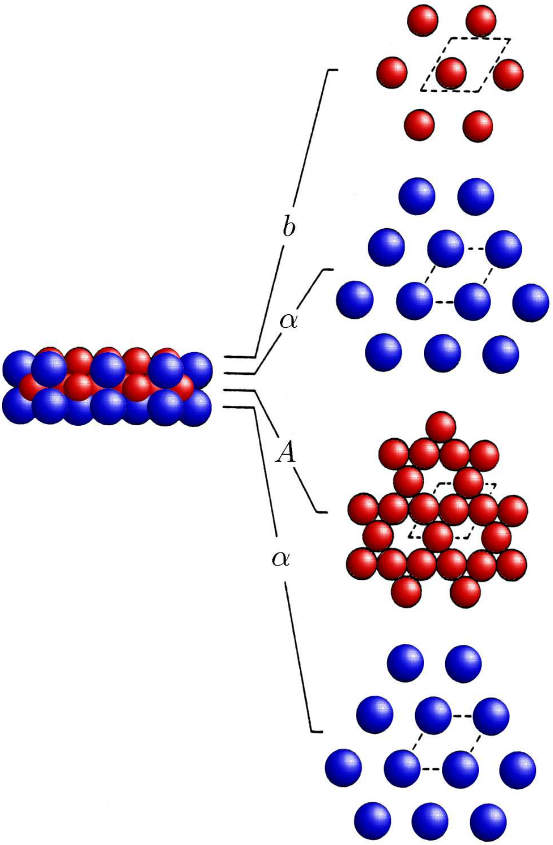

Figure 1.2: The basic four-layer stacking unit $\alpha\, A\, \alpha\, b$ of the Friauf-Laves phase structures (from [76], modified).

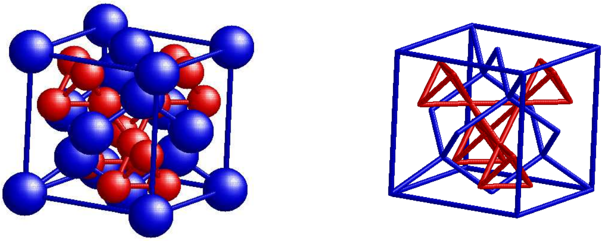

Figure 1.3: The C15 Friauf-Laves phase. Nearest neighbors of the same kind are connected by lines. The cubic cell containing 24 basis atoms is also indicated.

Chapter 2

Fracture mechanics

Condensed matter under heavy load can fail by fracture. Cracks propagate – mostly from pre-existing defects – by breaking cohesive bonds between atoms. At the macroscopic scale, the geometry of the sample and its dimensions determine the stress concentration at a crack tip.

2.1 Linear elastic theory

In linear elastic fracture mechanics the specimen is treated as an elastic continuum. Cracks are represented by free, plane surfaces. The crack front is approximated as a straight line. Following Irwin [56], the strain field of a crack can be split into contributions from three loading conditions: an opening (I), a sliding (II), and a tearing (III) mode (see figure 2.1). Friction is neglected, although in modes II and III the fracture surfaces stay in contact.

For a semi-infinite crack in an infinite plate of homogeneous, isotropic material the components of the stress tensor T_{ij} and the displacements u_i for mode m are given by (see, e.g., [36, 106]):

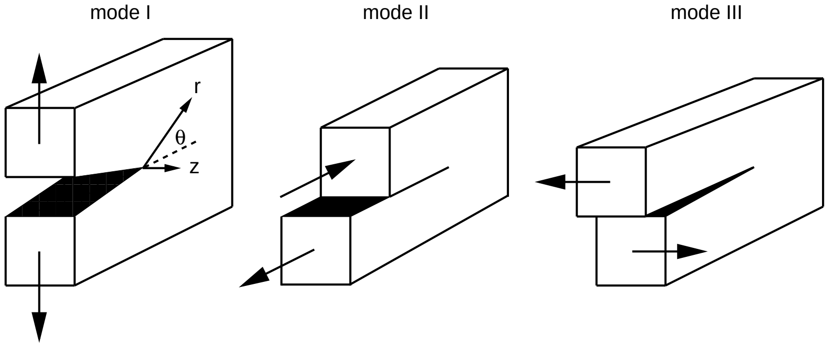

Figure 2.1: The three modes of crack loading.

$$T_{ij}^m(r,\theta) = \frac{K^m}{\sqrt{r}} f_{ij}^m(\theta)\,, \tag{2.1}$$

$$u_i^m(r,\theta) = K^m \sqrt{r} g_i^m(\theta)\,. \tag{2.2}$$

Here, r is the distance from the crack tip and θ is the angle between the fracture plane and the corresponding position vector $\mathbf{r}$ (see figure 2.1). The stress field carries a singularity at the crack tip that decays as the inverse square root of r. The strength of this singularity is characterized by the stress intensity factor K. It includes the applied external load and the geometry of the sample. The dependency on θ is contained in the functions f_{ij} and g_i. In general, they further depend on the orientation of the system via appropriate elastic constants.

For very thin samples ($z \to 0$) in mode I the stress field can be regarded as two-dimensional. Thus, this case is called plane stress. In contrary, for very thick samples ($z \to \infty$) the displacement field becomes two-dimensional and plane strain conditions are applicable.

When a crack moves through a solid, energy flows into the crack tip. The elastic work delivered by the specimen per unit area of crack advance is named energy release rate G. For mode m it is given by (see, e.g., [36, 106]):

$$G^m = (K^m)^2 / C^m\,, \tag{2.3}$$

where C^m is an appropriate elastic modulus.

2.2 The Griffith criterion

From the above equations it is possible to describe an idealized, sharp crack in an elastic medium. However, to decide whether a specimen fails or not, an additional criterion is needed. Following Griffith [40] one may assume that the static crack is a reversible thermodynamic system. The corresponding equilibrium condition for the system then simply follows from energy conservation. An unstable equilibrium is reached if the crack driving force, the energy release rate G, balances the surface energy of the two freshly exposed surfaces 2γ:

$$G_{\text{Griffith}} = 2\gamma\,. \tag{2.4}$$

For $G > G_{\text{Griffith}}$ the idealized crack opens up, for $G < G_{\text{Griffith}}$ the crack closes.

2.3 Propagating cracks

For propagating cracks the kinetic energy of the material has to be taken into account. A simple approximation by Mott [82] shows that there exists an upper limit for the crack velocity v_{crack}. Stroh [104] argumented that this velocity should be given by the Rayleigh wave speed. In a more elaborate approach (see, e.g., [36]) the dynamic stress intensity factors differ by a velocity dependent part from the static ones. As a consequence, the dynamic energy release rate vanishes when the limiting velocity is reached.

Yoffe [117] calculated the component $T_{\theta\theta}$ for a moving crack to decide on its kinetic stability. In the static case $T_{\theta\theta}$ is maximal for $\theta = 0$. However, if a crack reaches about 60% of the transverse wave velocity the maximum is shifted towards ±60°. Thus, a crack then might be expected to propagate off-axis.

2.4 Effects of discrete structures

From an atomistic point of view, brittle fracture is ultimately determined by the breaking of bonds. The discrete nature of matter, however, is fully neglected in a continuum description. Such an approach therefore is not capable of explaining fundamental processes on the atomic level. Additionally, the linear elastic approximation loses validity close to the crack tip, which is also apparent from the stress singularity (see Sec. 2.1).

Bonds are broken successively as a crack propagates (see figure 2.2). Following Griffith, the energy consumed for brittle fracture increases linearly with the generated surface or the position of the crack tip (dashed line in figure 2.2). However, in a simple atomistic picture energy only

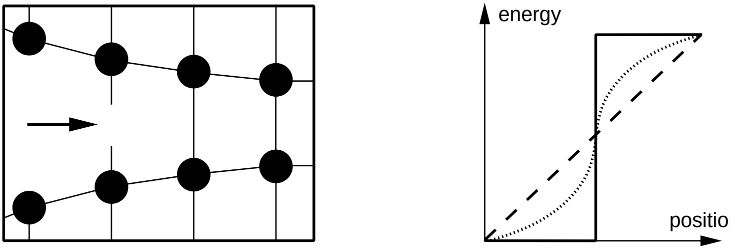

Figure 2.2: Energy required for crack propagation (schematic drawing).

is required to break bonds at discrete positions (solid curve in figure 2.2). A somewhat more realistic case is drawn in between in figure 2.2. Obviously, the arrangement of atoms close to the crack tip and the form of the interatomic force law (see, e.g., [41]) can influence crack propagation.

Thomson [107] showed that due to the discreteness of the lattice cracks remain stable even under loads that deviate from the Griffith value K_{Griffith}. This effect is called lattice-trapping. It also can cause an anisotropy with respect to the propagation direction on one and the same cleavage plane. Another consequence is that cleavage does not necessarily lead to surfaces with lowest energy (see, e.g., [43]).

2.5 Brittleness and ductility

Up to now perfectly brittle materials have been investigated. However, plastic deformation accompanies and competes with fracture. Whether a material essentially behaves ductile or brittle depends on the ability to nucleate and emit dislocations from a crack tip or from other sources. Dislocations can impede crack motion in three ways: First, they dissipate energy. Secondly, their stress field can shield the forces acting on a crack tip. Thirdly, they also may blunt a crack tip.

Following Kelly [64], materials are fully brittle if the ratio of the largest tensile stress to the largest shear stress close to the crack tip is larger

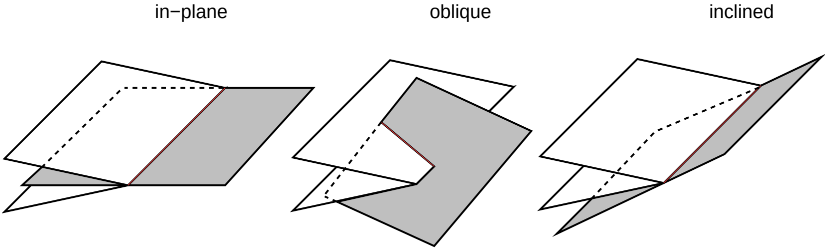

Figure 2.3: Possible orientations of a slip plane.

than the ratio of the ideal[1] cleavage stress to the ideal[1] shear stress. Rice and Thomson [90] calculated the force on a fully formed blunting dislocation in the presence of a crack. It follows that a straight dislocation is in unstable equilibrium at a critical distance. A crack is regarded as stable against dislocation emission if this value is smaller than a characteristic core cut-off radius. Rice [89] further analyzed dislocation formation using the Peierls concept. The resistance to dislocation nucleation in this concept is characterized by the so-called unstable stacking (fault) energy γ_{us}.

The orientation of the slip planes also influences the ability to nucleate and emit dislocations from a crack tip. For isotropic solids under mode I loading and plane strain conditions inclined planes (see figure 2.3) experience high shear stress values (see, e.g., [16]).

---

[1] The ideal values are estimated theoretical strengths of the materials.

Chapter 3

Numerical methods

Experiments are the foundation of science. Their results help to interpret and understand fundamental physical principles and laws. Numerical calculations and simulations help to assist, to interpret, and sometimes even to substitute real experiments. Ab-initio calculations (see, e.g., [63, 65, 85]) can predict material properties to a high accuracy. However, they are limited to samples with a few hundreds of atoms. On the other hand, classical molecular dynamics simulations (see, e.g., [6, 45]) can deal with millions of atoms without problems. But these then require effective potentials (see section 3.2.1) to mimic the interactions between the particles.

3.1 Ab-initio calculations

The Hamiltonian $\hat{H}$ of the non-relativistic Schrödinger equation for a many-particle system is given by

$$\hat{H} = \hat{H}_\mathrm{e} + \hat{H}_\mathrm{n} + V_\mathrm{en} \,, \tag{3.1}$$

where $\hat{H}_\mathrm{e}$ and $\hat{H}_\mathrm{n}$ contain the kinetic energies and the Coulomb interactions of the N_e electrons:

$$\hat{H}_\mathrm{e} = \hat{K}_\mathrm{e} + V_\mathrm{e} = \sum_{i=1}^{N_\mathrm{e}} \frac{\hat{\mathbf{p}}_i^2}{2m} + \frac{1}{2} \sum_{i=1}^{N_\mathrm{e}} \sum_{\substack{j=1 \\ (j \neq i)}}^{N_\mathrm{e}} \frac{e^2}{|\mathbf{r}_i - \mathbf{r}_j|} \tag{3.2}$$

and the N_n nuclei with the charge $Z_i e$:

$$\hat{H}_\mathrm{n} = \hat{K}_\mathrm{n} + V_\mathrm{n} = \sum_{i=1}^{N_\mathrm{n}} \frac{\hat{\mathbf{P}}_i^2}{2M_i} + \frac{1}{2} \sum_{i=1}^{N_\mathrm{n}} \sum_{\substack{j=1 \\ (j \neq i)}}^{N_\mathrm{n}} \frac{Z_i Z_j \, e^2}{|\mathbf{R}_i - \mathbf{R}_j|} \,. \tag{3.3}$$

Whereas $\hat{V}_\mathrm{en}$ determines the interactions between the electrons and the nuclei:

$$V_{\mathrm{en}} = -\sum_{i=1}^{N_{\mathrm{n}}}\sum_{j=1}^{N_{\mathrm{e}}} \frac{Z_i\, e^2}{|\mathbf{R}_i - \mathbf{r}_j|}\,. \tag{3.4}$$

$\hat{\mathbf{P}}_i$ and $\hat{\mathbf{p}}_i$ are the momentum operators of the nuclei and the electrons. The corresponding positions are $\mathbf{R}_i$ and $\mathbf{r}_i$. The normalized eigenfunction Ψ of $\hat{H}$ depends on the positions and spins of all electrons and nuclei. The total energy E of the system then is:

$$E = \langle \Psi | \hat{H} | \Psi \rangle\,. \tag{3.5}$$

The wave function Ψ_0 that minimizes E defines the ground state of the system.

The mass M_i of an atomic nucleus is at least three orders of magnitude bigger than the mass m of an electron. Therefore, the electrons move much faster than the nuclei. In the adiabatic approximation [14] the electrons instantaneously follow the nuclei and stay in their ground state. The energy of this electronic ground state can be determined with the help of density functional theory [66] for given positions of the nuclei. In a further approximation the nuclei move like classical particles. The forces on them then can be calculated with the help of the Hellmann-Feynman theorem [35].

3.1.1 Density functional theory

Hohenberg, Kohn, and Levy [51, 74] showed that the energy of an interacting electron gas in an external potential is a functional of the electron density. This functional is minimized by the correct ground-state electron density n and then equals the ground-state energy. Kohn and Sham [67] introduced a fictitious system of non-interacting particles that generate the same electron density as the interacting system. These Kohn-Sham particles fulfill the Kohn-Sham equations:

$$\left\{ -\frac{\hbar^2}{2m}\nabla^2 + v_{\mathrm{eff}}(\mathbf{r}) \right\} \varphi_i(\mathbf{r}) = \epsilon_i \varphi_i(\mathbf{r})\,. \tag{3.6}$$

The effective potential v_{eff},

$$v_{\text{eff}}(\mathbf{r}) = v_{\text{ext}}(\mathbf{r}) + v_{\text{H}}(\mathbf{r}) + v_{\text{xc}}(\mathbf{r})\,, \tag{3.7}$$

is a sum of the external potential v_{ext},

$$v_{\text{ext}}(\mathbf{r}) = -\sum_{i=1}^{N_{\text{n}}} \frac{Z_i\, e^2}{|\mathbf{R}_i - \mathbf{r}|}\,, \tag{3.8}$$

the Hartree potential v_{H},

$$v_{\text{H}}(\mathbf{r}) = e^2 \int \frac{n(\mathbf{r}')}{|\mathbf{r} - \mathbf{r}'|}\, d^3r'\,, \tag{3.9}$$

and the exchange-correlation potential v_{xc}, which combines all the remaining contributions that allow to map the many-particle problem on the effective one-particle Schrödinger equation 3.6. The electron density n results from

$$n(\mathbf{r}) = \sum_{i=1}^{N_{\text{e}}} |\varphi_i(\mathbf{r})|^2\;. \tag{3.10}$$

With the self-consistent solution, the ground-state energy now can be derived from the energy functional. However, the form of the exchange-correlation potential is still unknown. In the local density approximation (LDA) [67] the exchange-correlation part is approximated at each position by a value arising from a homogeneous free-electron gas with the same density. An extension to this method is the generalized gradient approximation (GGA) (see, e.g., [65] and references therein).

3.1.2 Plane-wave basis

According to Bloch's theorem a wavefunction φ_l in a periodic external potential can be written as:

$$\varphi_l(\mathbf{r}) = \varphi_{j\mathbf{k}}(\mathbf{r}) = e^{i\mathbf{k}\mathbf{r}} u_{j\mathbf{k}}(\mathbf{r})\,, \tag{3.11}$$

where the function $u_{j\mathbf{k}}$ has the same periodicity as the lattice. Thus, this part can be expanded using plane waves with reciprocal lattice vectors $\mathbf{G}$:

$$\varphi_{j\mathbf{k}}(\mathbf{r}) = \sum_{\mathbf{G}} c_{\mathbf{G}}^{j\mathbf{k}}\, e^{i(\mathbf{k}+\mathbf{G})\mathbf{r}}\,. \tag{3.12}$$

All sums over occupied one-particle states now are transformed into sums over $\mathbf{k}$ vectors and band indices j in the first Brillouin zone. Due to the N_{e} index combinations, the summation can be replaced by an integration, which in turn can be approximated by a summation over selected nodes. One method to obtain a representative special set of $\mathbf{k}$ points was invented by Monkhorst and Pack [80].

In general, an infinite basis set is required for the expansion in equation 3.12. But typically only coefficients $c_{\mathbf{G}}^{j\mathbf{k}}$ with small kinetic energy $\frac{\hbar^2}{2m}\,|\mathbf{k}+\mathbf{G}|^2$ are important. Hence, the plane-wave basis set can be truncated at a finite cutoff energy.

3.1.3 Valence and core electrons

The physical properties of bulk solids often are determined to a greater extent by the valence electrons than by the core electrons. In the frozen-core approximation, it may further be assumed that the localized core orbitals are independent of the chemical environment [112]. In a region occupied by the core electrons the valence wave functions show rapid oscillations. This is due to the strong ionic potential and due to the orthogonality constraints, which arise from the exclusion principle. Thus, a very large number of plane waves would be required to expand both the tightly bound core orbitals and the oscillating valence electrons. Several methods have been devised to circumvent this problem.

In the pseudopotential (PP) approach [46, norm-conserving] [110, ultrasoft] the core electrons and the ionic potential are replaced within a certain region by a pseudopotential. The corresponding pseudo wave functions agree with the true wave functions outside this region. Inside, they can be very smooth. In the linear all-electron methods [8, LAPW (linear augmented-plane-wave) / LMTO (linear muffin-tin orbital)], the wavefunction is expanded in a variable basis set, which is atomic-like in the vicinity of the atoms and more general elsewhere. The projector augmented-wave (PAW) concept [12, 69] combines ideas from the PP and the LAPW methods.

3.2 Molecular dynamics simulations

The Hamiltonian for a configuration of N classical particles shall be given by:

$$H(\mathbf{P},\mathbf{R}) = K(\mathbf{P}) + U(\mathbf{R}) , \tag{3.13}$$

where $\mathbf{R} = (\mathbf{R}_1, ..., \mathbf{R}_N)^{\mathrm{T}}$ and $\mathbf{P} = (\mathbf{P}_1, ..., \mathbf{P}_N)^{\mathrm{T}}$ contain the position vectors $\mathbf{R}_i$ and the momenta $\mathbf{P}_i$ of all particles. U is the potential energy and K the kinetic energy:

$$K(\mathbf{P}) = \sum_{i=1}^{N} \frac{\mathbf{P}_i^2}{2M_i} . \tag{3.14}$$

The equations of motion in the Hamiltonian form then become:

$$\dot{\mathbf{R}}_i = \frac{\mathbf{P}_i}{M_i} , \quad \dot{\mathbf{P}}_i = -\nabla_{\mathbf{R}_i} U = \mathbf{F}_i . \tag{3.15}$$

$\mathbf{F}_i$ is the force on particle i with the mass M_i. Time is discretized to numerically integrate these equations. The Taylor expansions of the coordinates and velocities $\mathbf{V}_i$ help to calculate these values at a later time. One of the various finite difference methods used is the half-step leap-frog scheme (see, e.g., [6]). The trajectories of the particles so can be approximated in a stepwise manner by applying a sufficiently small time step.

3.2.1 Effective potentials

The potential energy may be broken up into contributions from individual particles, pairs, triplets, etcetera. If only the pair terms are taken into account, the potential energy can be written as:

$$U = U_2 = \sum_{i,j<i}^{N} \phi_{k_i k_j}(r_{ij}) . \tag{3.16}$$

The pair potential $\phi_{k_i k_j}$ may then depend only on the distance $r_{ij} = |\mathbf{R}_i - \mathbf{R}_j|$ between the particles i and j. The species is denoted by k_i. A more sophisticated approach for metals is the embedded atom method

(EAM) [25, 26]. Following the EAM formalism an embedding term is added to the potential energy:

$$U_{\mathrm{EAM}} = U_2 + \sum_{i}^{N} F_{k_i}(\rho_i^h)\,, \quad \rho_i^h = \sum_{j\neq i}^{N} P_{k_j}^{at}(r_{ij})\,. \tag{3.17}$$

The embedding function F_{k_i} depends on the host density ρ_i^h of atom i, which is a sum over the transfer functions $P_{k_j}^{at}$ of the neighboring atoms j. In a physical interpretation, the additional terms arise from embedding the host particle in a sea of "electrons" provided by the neighboring atoms. Thus, many-body interactions without explicit angular dependences are included. It is often stated that the pair term represents the core repulsion. However, because of gauge degrees of freedom, the "core" and "electronic" contributions are not uniquely defined. In an extended EAM scheme [10, 116] further embedding functions M_{k_i} are included, which depend on the sum q_i^h of the squared transfer functions:

$$U_{\mathrm{eEAM}} = U_{\mathrm{EAM}} + \sum_{i}^{N} M_{k_i}(q_i^h)\,, \quad q_i^h = \sum_{j\neq i}^{N} \Big(P_{k_j}^{at}(r_{ij})\Big)^2\,. \tag{3.18}$$

The pair potentials, the embedding functions, and the transfer functions determine the interactions and thus the chosen material. Simple model potentials can help to get insight into fundamental mechanisms without being specific to a single material. Often, they already resemble well essential features of real physical systems. In a further step the potential functions can be fitted to properties known from experiment or from ab-initio calculations. Ercolessi and Adams [33] proposed to generate potentials that reproduce ab-initio forces of many configurations. Such effective potentials then help to acquire material properties quantitatively.

For large distances r_{ij} the corresponding potential functions vanish. Thus, they can be set to zero at and beyond a finite cut-off radius r_{cut}. The functions should be continuous and continuously differentiable everywhere. Dividing the simulation box into cells with sufficient size, it can be guaranteed that a particle only interacts with other particles in the same cell or in the neighboring 26 cells [88].

3.2.2 Boundaries

In today's computer simulations a high percentage of the atoms is located at the sample boundaries. There are three main methods to handle the borders of the simulation box:

- **Free boundaries**
  Atoms at the borders possess fewer nearest neighbors and thus have a higher potential energy. Fluctuations may cause atoms at the boundaries to evaporate.

- **Fixed boundaries**
  The motion of atoms is restricted totally or only in some directions. If atoms inside a cut-off distance from the borders are fixed, the other atoms are not directly influenced by the boundaries.

- **Periodic boundaries**
  An infinitely extended sample without free surfaces can be realized if the simulation box is extended periodically in each direction. An atom leaving the box reenters through the opposite side. Ab-initio calculations with plane-wave basis make use of periodic boundaries. Defects are then simulated using supercells (see, e.g., [85]).

3.2.3 Statistical mechanics

In thermodynamic equilibrium, a system is characterized by a few macroscopic variables like temperature or pressure. The values obtained by equilibrium molecular dynamics simulations are microscopic quantities. From these the corresponding macroscopic variables can be derived with the help of statistical mechanics. In an ergodic system the average over the statistical ensemble can be replaced by the time average. The temperature T and the pressure P then can be written as follows:

$$T = \frac{2 < K(\mathbf{P}) >}{3Nk_\mathrm{B}}\,, \quad P = \frac{Nk_\mathrm{B}T + < \mathcal{V} >}{V}\,. \tag{3.19}$$

V is the volume, k_B is the Boltzmann constant. The brackets denote time averages. The internal virial $\mathcal{V}$ is given by:

$$\mathcal{V} = -\frac{1}{3}\sum_{i=1}^{N} \mathbf{R}_i \cdot \nabla_{\mathbf{R}_i} U \,. \tag{3.20}$$

Momentary values of temperature and pressure may be defined accordingly:

$$T_{\mathrm{mom}} = \frac{2K(\mathbf{P})}{3Nk_{\mathrm{B}}}\,, \quad P_{\mathrm{mom}} = \frac{Nk_{\mathrm{B}}T + \mathcal{V}}{V}\,. \tag{3.21}$$

3.2.4 Ensembles and relaxators

Macroscopic constraints define different ensembles. In computer simulations they can be realized as follows:

- **The microcanonical ensemble**
  The number of particles N, the volume V, and the energy E are conserved for the integration algorithm defined in section 3.2. Thus, an (N, V, E)-ensemble is realized.

- **The canonical ensemble**
  To arrive at the (N, V, T)-ensemble a thermostat has to be included in the equations of motion [7, 54, 55, 83]:

$$\dot{\mathbf{R}}_i = \frac{\mathbf{P}_i}{M_i}\,, \quad \dot{\mathbf{P}}_i = \mathbf{F}_i - \xi \mathbf{P}_i \,. \tag{3.22}$$

  Here ξ should cause the momentary temperature T_{mom} to approach T. This is achieved if

$$\dot{\xi} \propto (T_{\mathrm{mom}} - T)\,. \tag{3.23}$$

- **The isothermal-isobaric ensemble**
  For the (N, P, T)-ensemble a barostat has to be introduced [7, 83] in addition to the thermostat. For this purpose, scaled coordinates are inserted in the equations of motion:

$$\dot{\mathbf{R}}_i = \frac{\mathbf{P}_i}{M_i} + \zeta \mathbf{R}_i \,, \quad \dot{\mathbf{P}}_i = \mathbf{F}_i - (\dot{\zeta} + \xi)\mathbf{P}_i \,. \tag{3.24}$$

The pressure P is maintained if

$$\dot{\zeta} \propto \frac{V}{T} (P_{\text{mom}} - P) \,. \tag{3.25}$$

The following relaxators help to achieve a final state with minimal potential energy. This is realized by a modification of the microcanonical ensemble.

- **Micro convergence (MIK)**
  Before each integration step, it is checked for each atom i if the scalar product $\mathbf{P}_i \cdot \mathbf{F}_i$ is smaller than zero. If so, its momentum is set to zero: $\mathbf{P}_i = \mathbf{0}$. The potential energy so is successively removed from the system unless a local minimum is obtained.

- **Global convergence (GLOK)**
  The global potential energy minimum can be found if now $\mathbf{P} \cdot \mathbf{F}$ (as defined in section 3.2) is considered instead of $\mathbf{P}_i \cdot \mathbf{F}_i$.

3.2.5 Fracture studies

A propagating crack emits phonons. These can be reflected at the sample boundaries and then disturb the motion of the crack. Therefore, Holian and Ravelo [52] proposed a method to absorb these sound waves. The geometry of the sample is shown in figure 3.1. The side lengths of the specimen are L_x, L_y, and L_z. Inside an elliptical cylinder with semi-major axis l_x, standard Newtonian mechanics applies. The cylinder is centered at $(x_0, y_0)^{\mathrm{T}}$ in the x-y-plane. Approaching the boundaries, the damping is increased by the elliptical stadium function [44, 118]

$$d(x,y) = \min\left[1, \max\left(0, \frac{\left(\frac{x-x_0}{L_x}\right)^2 + \left(\frac{y-y_0}{L_y}\right)^2 - \left(\frac{l_x}{L_x}\right)^2}{\frac{1}{4} - \left(\frac{l_x}{L_x}\right)^2}\right)\right] \,. \tag{3.26}$$

The strength of the damping

$$\eta = 2\omega_{\mathrm{E}} \left(1 - \frac{T_0}{\tau}\right) d(x,y) \tag{3.27}$$

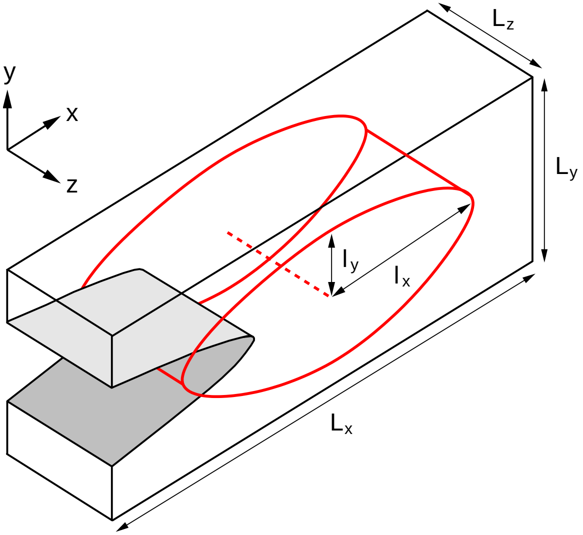

Figure 3.1: Sketch of the simulation set-up.

ensures that

$$\tau = \frac{\sum_{i=1}^{N} d(x,y)\, M_i \mathbf{V}_i^2}{3k_{\mathrm{B}} \sum_{i=1}^{N} d(x,y)} \tag{3.28}$$

reaches a given temperature T_0. The equations of motion are

$$\dot{\mathbf{R}}_i = \frac{\mathbf{P}_i}{M_i}\,, \quad \dot{\mathbf{P}}_i = \mathbf{F}_i - \eta \mathbf{P}_i\,. \tag{3.29}$$

An atom in the mean force field of its neighbors vibrates in harmonic approximation with the Einstein frequency

$$\omega_{\mathrm{E}} = \sqrt{\frac{< \mathbf{F}_i^2 >}{M_i^2 < \mathbf{V}_i^2 >}}\,. \tag{3.30}$$

Sample preparation

A sample form is chosen that makes it possible to follow the dynamics of the running crack for a long time. For this purpose, a strip geometry (see figure 3.1) is used to model crack propagation with constant energy release rate [44] (see also section 2.1). The samples consist of about 4 to 5 million atoms. The length of the strips L_x is set to about 0.1 µm. The dimensions of the samples are approximately $L_x \times \frac{L_x}{3} \times \frac{L_x}{6}$. Periodic boundary conditions are applied in the direction parallel to the crack front. For the other directions, all atoms in the outermost boundary layers of width r_{cut} are held fixed. An atomically sharp seed crack is inserted in the relaxed samples at a plane of lowest surface energy from one side to about $L_x/4$. The system is uniaxially strained perpendicular to the crack plane up to the Griffith load (see section 2.2) and is relaxed to obtain the displacement field of a stable crack at zero temperature. As we want to explore dynamic fracture without strong thermal fluctuations, we apply a temperature[1] of about 10^{-4} of the melting temperature to the configurations with[2] and without the relaxed crack. From the resulting configurations we obtain an averaged displacement field for this temperature. The mode I crack (see figure 2.1) then is further loaded by linear scaling of the displacement field. The response of the system is monitored using the above equations. The sound waves emitted by the propagating crack so are damped away outside of an elliptical stadium to prevent reflections.

Visualization

Due to the large number of atoms required for the study of dynamic fracture in three-dimensional systems, it is not feasible to always write out the positions of all particles during the simulation. To obtain a first insight, only the fracture surfaces are of interest. These can be visualized in periodic crystals by plotting atoms whose potential energy exceeds a certain threshold[3]. Alternatively, particles can be displayed, which exhibit a coordination number that is smaller than a certain threshold (see figure 3.2). As atoms near defects have a significantly lower coordination number, it becomes possible to visualize fracture surfaces and dislocation cores. With this method, the number of atoms to write out or to display can be reduced by three orders of magnitude. From the

---

[1] Equations (3.27)–(3.29) with $d \equiv 1$ are used.

[2] Subsequently, a simulation with the correct stadium function d is run.

[3] However, this technique is not applicable for quasicrystals. Because of the largely varying environments, the potential energy varies significantly from atom to atom, even for atoms of the same type in a defect-free sample.

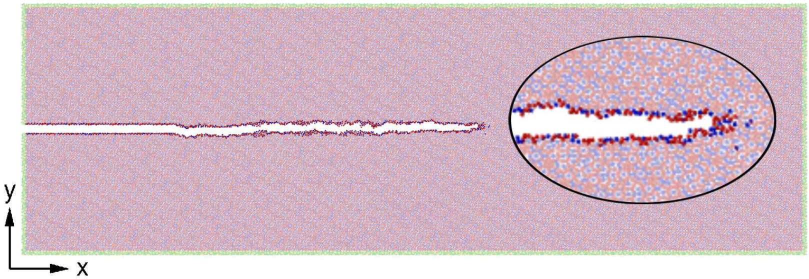

Figure 3.2: Atoms with unusual coordination number form the fracture surfaces. All other atoms are shown in faded colors.

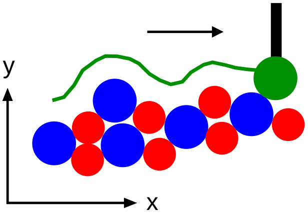

Figure 3.3: Geometrical scanning of the fracture surfaces.

obtained data, it is also possible to evaluate the velocity of the crack. The morphology of the fracture planes is analyzed via geometrical scanning[4] (see figure 3.3) of the atoms forming the surfaces. The roughness can be visualized by color coding the height of the surface in a view normal to the fracture plane.

Abbreviations

To characterize the applied load, the reduced stress intensity factor k is defined as the ratio of the stress intensity factor K to the Griffith value K_{Griffith} (see sections 2.1 and 2.2):

$$k = \frac{K}{K_{\text{Griffith}}} \,. \tag{3.31}$$

---

[4] The scanning is performed with a Y atom at equidistant points separated by 0.5Å.

To identify the orientations of the samples the notation

$$y_x \tag{3.32}$$

is introduced. Here y is an axis perpendicular to the cleavage plane and x is an axis in the crack propagation direction (see figure 3.1). An f-fold axis is denoted by the number f.

Chapter 4

Results and discussion

Many fracture simulations are performed with simplified interaction laws and model systems (see, e.g., [1]). This approach helps to understand elementary processes of crack propagation and is reasonable when qualitative mechanisms are the center of interest. Furthermore, most of the available realistic effective potentials are fitted to simple monoatomic systems and their equilibrium properties. For complex metallic alloys (CMAs) reliable potentials are practically inexistent.

The effect of the structure on fracture behavior is investigated with model potentials in section 4.1. Two extreme cases of CMAs are studied: In a model quasicrystal the structure is determined by clusters of atoms, whereas the model C15 Friauf-Laves phase is a simple periodic stacking of a unit cell (see chapter 1).

For the main part of this work, a specific material is chosen in section 4.2. Effective potential functions are generated by matching them to ab-initio data from C15 $NbCr_2$. The interactions are used for fracture studies on differently oriented samples under diverse loads.

4.1 Model systems

Lennard-Jones pair potentials (see figure 4.1) are chosen for the interactions of the model systems. These potentials keep the icosahedral binary model stable even under strong mechanical deformation or irradiation[1] and have been used in many simulations of dislocation motion [99] or even shock waves [97]. Very similar interactions have shown to stabilize the icosahedral atomic structure in a simpler model [98]. Because of the close structural relationship between the model quasicrystal and the Friauf-Laves phase (see chapter 1) the potentials can be applied in both cases.

---

[1] Point defects are introduced.

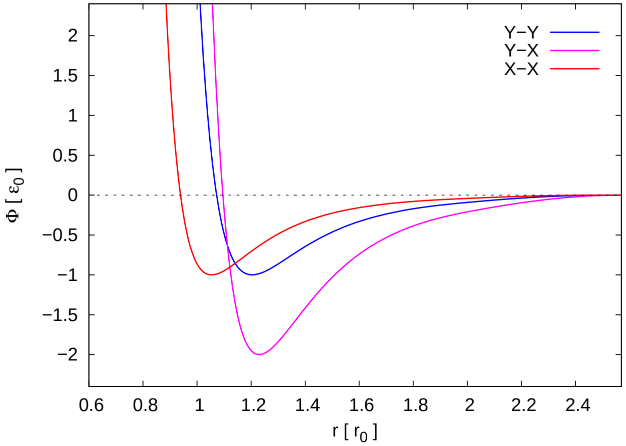

Figure 4.1: Lennard-Jones pair potentials.

The minima of the potentials for interactions between atoms of the same type are set to ϵ_0, whereas the minimum of the potential for the interactions between atoms of different kind is set to $2\epsilon_0$. The shortest distance between two X atoms (see chapter 1 and figure 1.1) is denoted r_0. All masses are set to m_0. The time is then measured in units of $t_0 = r_0\sqrt{m_0/\epsilon_0}$.

Using appropriate model potentials, the overall qualitative behavior of the structures should be represented well. However, results certainly will differ quantitatively for diverse materials (interactions), even for compounds with the same crystal lattice structure. Especially, the lattice-trapping effect (see section 2.4) strongly depends on the applied force law.

All molecular dynamics simulations were carried out with the ITAP molecular dynamics program IMD [102, 119]. It performs well on a large variety of hardware, including single and dual processor workstations and massively parallel supercomputers.

4.1.1 Model quasicrystal

Fundamental results on the fracture behavior of the binary model quasicrystal were obtained during the diploma thesis of the present author [91]. Major findings from this work and some newer aspects [92, 94] are reported here and compared to simulation results on the model Friauf-Laves phase [94]. The goal of the sections 4.1.1 and 4.1.2 is to provide a qualitative insight into the fracture behavior of model CMAs with different structural complexity.

The model quasicrystal fails by brittle fracture without any crack tip plasticity irrespective of the orientation of the fracture plane. For loads below $k = 1.2$ the crack propagates at most a few atomic distances, and then stops. Thus, the energy required for initiating crack propagation is about 1.4 times the value predicted by the Griffith criterion (see section 2.1). This behavior can be assigned to the lattice-trapping effect (see section 2.4).

Simulated fracture surfaces (see section 3.2.5) of the model quasicrystal are displayed in figure 4.2. The average height is shown in gray, heights above $+2r_0$ are shown in white and heights below $-2r_0$ are shown in black. The crack propagation direction is from the left to the right. The surfaces of the seed cracks[2] are flat, as can be seen from the homogeneous regions on the left. The propagating crack, however, generates surfaces with pronounced patterns of regions with different heights. The peak-to-valley roughness[3] is about $4r_0$ which corresponds to the diameter of the Bergman-type clusters (see figure 1.1).

Fracture surfaces perpendicular to a fivefold axis are shown in the middle and bottom of figure 4.2. The initial seed cracks are inserted at the same cleavage plane. Thus, their surface energies are identical. However, the in-plane crack propagation directions differ[4]. As can be seen in figure 4.2 the corresponding fracture surfaces also vary. For the orientation 5_{p2} ledges are produced, while no ledges form for the orientation 5_2. These ledges and the observed markings (see also figure 4.2, top) in

---

[2] These have been chosen as planes of low surface energy.

[3] for the surfaces without ledges

[4] Pseudo-twofold (p2) axes are perpendicular to fivefold (5) and twofold (2) axes.

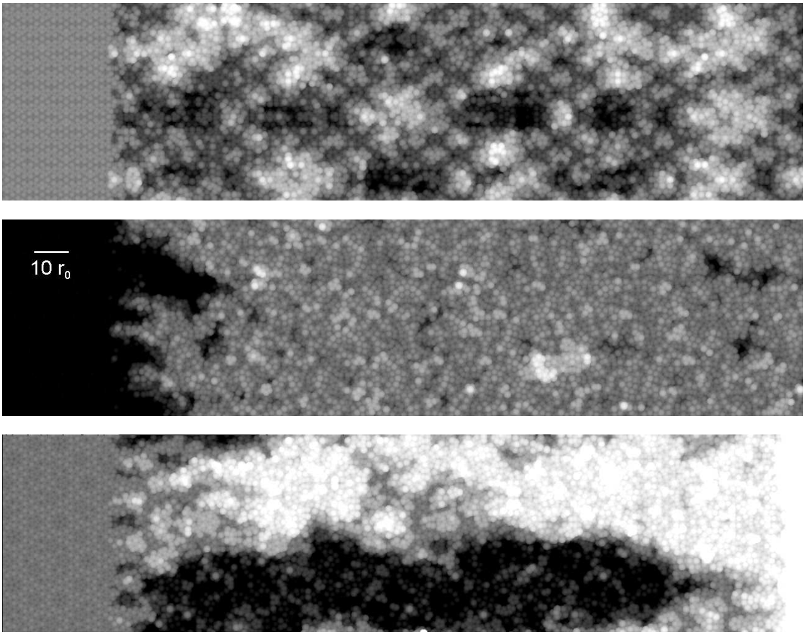

Figure 4.2: Height profiles of fracture surfaces of the model quasicrystal [92]. Load: $k = 1.3$, orientation: 2_2 (top), 5_2 (middle), $5_{\mathrm{p}2}$ (bottom).

the fracture surfaces can be related to lines along which the clusters are located. The associated angles are determined by the symmetry and thus reveal the orientation of the sample.

Figure 4.3 displays from bottom up: The density of the cluster centers, the surface energy, a cluster in the proper length scale, the gray coding of the heights (for figure 4.2, middle), and the position of the seed crack (dashed vertical line). The figure shows that the seed crack is situated close to a peak of the cluster density. Obviously, it is not possible to circumvent all clusters by a planar cut. The gray coding is adjusted to the average height of the fracture surfaces. Thus, it is evident from figure 4.3 and figure 4.2 that the crack deviates for the orientation 5_2

from the low energy cleavage plane of the seed crack to a parallel plane[5]. Samples cut flat at this height show a slightly higher surface energy[6] (see figure 4.3). However, the number of cluster intersections is reduced dramatically[7]. This is visualized in figure 4.4. Only the smaller parts of those clusters are displayed that were divided by the crack. Obviously, the dynamic crack (right) intersects fewer clusters than the low energy seed crack (left). Thus, there seems to be an influence of the clusters on the crack path. Furthermore, dynamic cracks propagating in fivefold planes with few cluster intersections are faster than those in twofold planes, where the absolute number of cluster intersections is higher [92].

In conclusion, the atomistic structure of the samples strongly influences fracture behavior. The plane structure of the quasicrystal (see section 1.1) leads to fracture surfaces that show constant average heights. The distribution of the clusters seems to control the crack speed, the anisotropy with respect to the in-plane propagation direction, the surface roughness, the observed patterns in the fracture surfaces, and the fracture path. Less clusters are intersected by the propagating crack than by the flat low energy cleavage planes. The cracks sometimes even deviate to parallel planes to reduce the number of cluster intersections in spite of the higher energy required. The clusters, too, are a reason why the positions of the cleavage planes cannot be predicted by a simple energy criterion.

Figure 4.5 compares a geometrically scanned fracture surface to an STM-image of Ebert et al. [29, 30]. In the left picture, the atomically sharp seed crack can be seen on the top, whereas below this area the simulated fracture surface appears. The orientation of the sample is 2_2, the load was $k = 1.3$. The right picture shows an STM-image of icosahe-

---

[5] To assure that the dynamic crack is departing from the initial plane not in a random manner, the seed crack was built in at the position color coded as medium gray in figure 4.3. The resulting fracture surface had a similar roughness, but the crack did not change to a parallel plane.

[6] However, for low loads and low roughness the actual fracture surfaces of the dynamic cracks have about 5-15% higher energies than those of the low energy seed cracks.

[7] More detailed analyses for different orientations validate this statement. For the orientations perpendicular to twofold and fivefold axes at $k = 1.3$ the ratio of clusters cut by the dynamic crack to clusters intersected by flat cuts is approximately 0.6.

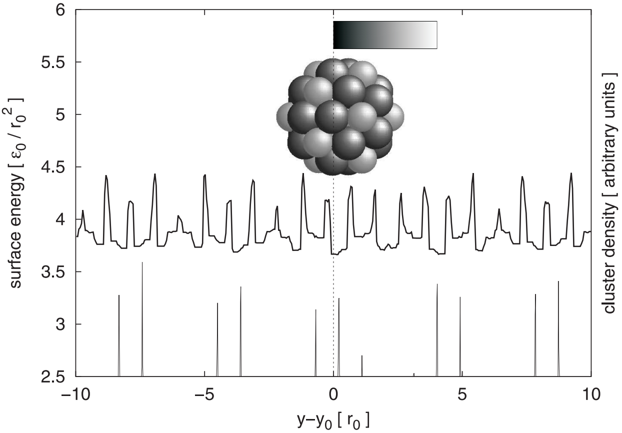

Figure 4.3: Density of cluster centers and surface energy for the orientation 5_2 [92]. The corresponding fracture surface is shown in figure 4.2, middle.

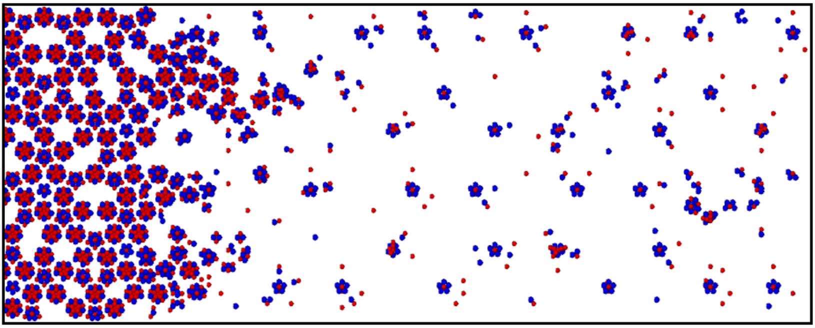

Figure 4.4: Clusters cut by a 5_2 crack in a model quasicrystal [94].

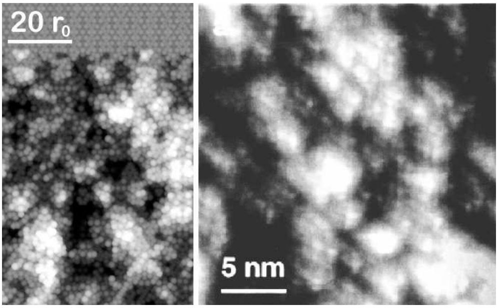

Figure 4.5: Fracture surfaces of quasicrystals perpendicular to twofold axes [92]. Left: simulation, right: experiment (adopted from [30]).

dral Al-Mn-Pd cleaved in ultrahigh vacuum. As $20\,r_0$ is approximately 5 nm, the surfaces are displayed at the same length scale. Al-Mn-Pd has a more complicated atomic structure than the icosahedral binary model and the clusters are not Bergman-type. However, the size of the clusters, the icosahedral symmetry, and a distinct plane structure are common features. Thus, qualitative aspects are reproduced well, namely the size and shape of the patterns and the appearance of distinct angles on the fracture surfaces. As it is possible to correlate the observed structures to the clusters in our model, the similarities corroborate the assumption that the clusters are also responsible for the globular structures observed in experiment.

Nevertheless, there is still an ongoing discussion whether the clusters are merely geometrical entities or also responsible for physical properties. The debate has been fueled by a recent article of Ponson et al. [86]. They measured the roughness exponent of the fracture surfaces of Ebert et al. and questioned a signature of the clusters. However, from height-height correlation functions of the simulated fracture surfaces and from a comparison to the experimental ones, one can conclude that the results of Ponson et al. cannot negate the role of the clusters in the fracture process [93]. Quite the contrary, the cluster structure of the quasicrystals can be used to interpret details of the correlation function. A profound discussion on this topic is given in the appendix.

4.1.2 Model Friauf-Laves phase

A fundamental building unit of the model quasicrystal – the prolate rhombohedron – in a slightly deformed way forms the cubic C15 Friauf-Laves phase by periodic arrangement (see chapter 1). No Bergman-type clusters are present in this structure. Brittle fracture is observed using the Lennard-Jones model interactions. The samples already fail at $k = 1.1$. This shows that the lattice-trapping effect does not only depend on the force law but also on the structure.

A $111_{2\bar{1}\bar{1}}$ seed crack (see figure 4.6, top) results in perfect brittle cleavage fracture for $k = 1.1$ (see figure 4.6, bottom). The surfaces are smooth. However, the fracture surfaces for 011_{100} and 010_{101} cracks at $k = 1.1$ are rough on an atomic scale. The fracture behavior is similar for the two cases. A time sequence for a propagating 011_{100} crack is illustrated in figure 4.7. If the seed crack there would be continued, the red lines would terminate the upper and lower halves of the sample. However, the dynamic crack instead takes a zig-zag like route. Entire atomic rows alternately move upwards and downwards. This leads to rather symmetric upper and lower fracture surfaces, the creation of which also requires a comparable amount of energy. These surfaces are favored, even though a planar cut would lead to surfaces with lower total energy[8]. Thus, the actual fracture path again cannot be predicted by a simple energy criterion. A similar behavior has been observed in B2 NiAl (see, e.g., [42]). The increased load for a crack to propagate also results in a surplus of energy. Thus, fracture surfaces are not necessarily those of lowest energy.

If the load is increased further, the fracture surfaces exhibit a more pronounced roughness. Additionally, the height profiles are no longer strictly periodical. This is illustrated in figure 4.8. On the left a 010_{101} fracture surface is displayed for $k = 1.3$, whereas on the right the load was $k = 1.1$. The color coding has been adjusted to visualize the different atomic planes.

Sections of typical fracture surfaces of the icosahedral model quasicrys-

---

[8] The increase in energy is about 6% for the 010_{101} crack and about 1% for the 011_{100} crack.

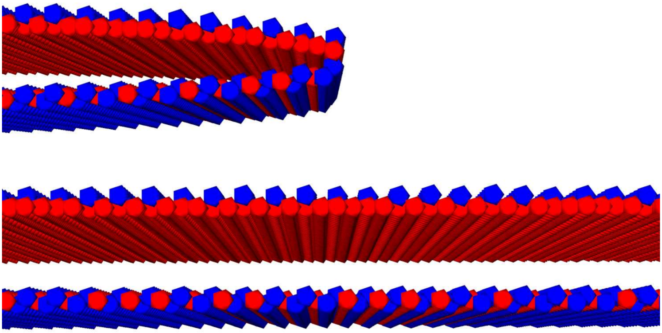

Figure 4.6: A $111_{2\bar{1}\bar{1}}$ crack in the C15 model Friauf-Laves phase [94].

tal and of the C15 model Friauf-Laves phase are compared in figure 4.9. The corresponding loads have been chosen to assure crack propagation. The side length of the squares is about 14 nm. The color coding in the left and middle picture has been adjusted to the diameter of the Bergman-type cluster (from blue to red). The fracture surfaces of the C15 Friauf-Laves phase lack any roughness when they are color coded like the quasicrystal (figure 4.9, middle). After adjusting the color coding, atomic rows become visible (figure 4.9, right). Thus, fracture surfaces of the quasicrystal are rough on the cluster scale, whereas those of the Friauf-Laves phase only are rough on an atomic scale.

In conclusion, the simulation results of the two extreme cases of model CMAs indicate that the basic building units of the structures also govern their fracture behavior. Atoms in the Friauf-Laves phase play a comparable role to the clusters in the quasicrystal – they determine the overall roughness of the fracture surfaces. The fracture path in the model materials is strongly influenced by the arrangement of atoms and clusters near the crack front. Therefore, not only the initial cleavage plane but also the crack propagation direction can have an influence on fracture behavior. The discrete nature of matter manifests itself in the lattice-trapping effect. Loads above the Griffith load are needed to allow crack propagation. This also causes excess energy. Thus, fracture surfaces are not implicitly those of lowest energy or lowest roughness.

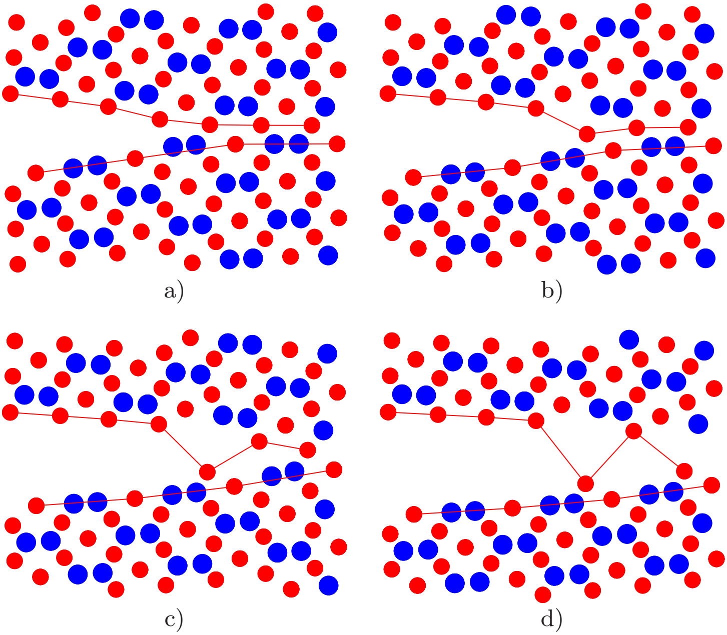

Figure 4.7: Fracture of the C15 model Friauf-Laves phase [94]: Atomic configurations in the vicinity of a propagating 011_{100} crack.

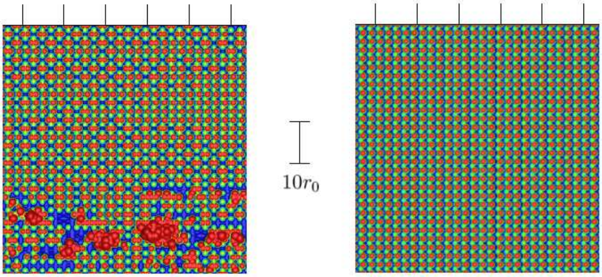

Figure 4.8: 010_{101} fracture surfaces of the C15 model Friauf-Laves phase. Left: $k = 1.3$, right: $k = 1.1$.

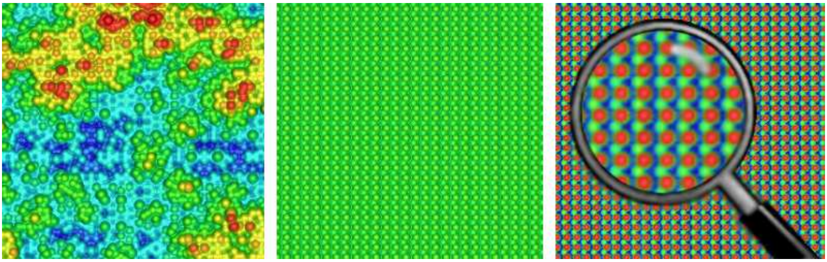

Figure 4.9: Fracture surfaces of the model quasicrystal (left; orientation 2_2, $k = 1.3$) and of the C15 model Friauf-Laves phase (middle, right; orientation 010_{101}, $k = 1.1$) [94].

4.2 C15 NbCr$_2$

The findings from the model systems allow a qualitative physical understanding of fracture behavior in CMAs. In materials science and engineering, however, quantitative results for specific materials often are the center of interest. Thus, this chapter will focus on a particular Friauf-Laves phase, namely C15 NbCr$_2$. Quantum mechanical calculations are performed on this compound to obtain reference data. Interatomic potentials are matched to reproduce these ab-initio values. The interactions are then applied to an extensive molecular dynamics study on crack propagation in NbCr$_2$.

A possible relevance for technical applications and the compatibility with EAM potentials guided the search for a specific material. Anomalous shear moduli and strong electron-phonon coupling e.g. exclude C15 HfV$_2$ and ZrV$_2$ [22]. Literature search lead to the choice of NbCr$_2$. Although the interatomic interactions are difficult to describe for the body-centered cubic (bcc) metals Nb and Cr [3, 5, 11, 34], these elements seem favorable for the simulation of the C15 Friauf-Laves phase because of the rather simple electronic [23, 84] and spatially close-packed structure of NbCr$_2$. Here, one has to point out that the potentials are matched for the Friauf-Laves phase and not for the elemental metals. Thus, the generated potentials may not be transferable to the elements.

4.2.1 Effective potentials

In a first step, forces, total energies, and stresses for diverse representative configurations are determined by ab-initio calculations. Density functional theory (DFT) calculations are performed within the generalized gradient approximation (GGA) for the exchange-correlation energy using the Vienna ab-initio simulation package VASP [68, 69, 122]. For Nb and Cr projector augmented-wave (PAW) potentials are applied, which treat the semi-core p states as valence. The maximal energy cutoff is increased by 30%. The samples consist of 24 to 144 atoms. The **k**-mesh is automatically generated using the Monkhorst-Pack scheme with up to 5 × 5 × 5 points. The 50 reference configurations include compressed, elongated, and sheared samples; vacancies are introduced and atoms are exchanged. Especially, calculations for free surfaces are carried out. To overcome the number of limited environments in ordered structures, samples at higher temperatures are used to obtain sufficient information on forces at various interaction distances. Furthermore, to get some sort of cohesion energy, the energies of single atoms in a triclinic box are calculated.

In the next step, the ab-initio data is used as input for the program potfit [17–19, 121], which has been developed by P. Brommer and F. Gähler. Following the force-matching method [33], the parameters of an effective potential are adjusted to optimally reproduce the ab-initio reference values. The program uses conjugate gradient [87] and simulated annealing [24] techniques within a least-squares method. The EAM potential functions are represented by splines. The number of sampling points used for the pair and transfer functions is typically about 15, the corresponding value for the embedding functions is about 10. To assure that the obtained potentials are defined even for extreme cases, they are manually extended: The pair potential for short distances with a term proportional to r_{ij}^{-12}, the transfer functions for short distances and the embedding functions for high densities with terms linear in r_{ij} and ρ_i^h. The thus obtained potential functions for $\mathrm{NbCr_2}$ are shown in figure 4.10. From now on the abbreviation “fm-EAM” is used for these force-matched interactions.

Additionally, analytical EAM potentials for the bcc metals Nb and Cr

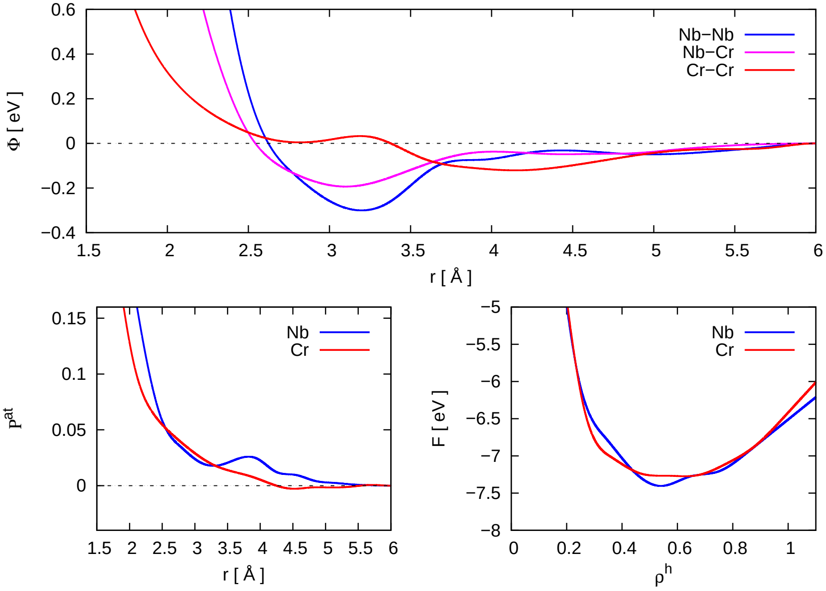

Figure 4.10: Force-matched EAM potential functions for NbCr$_2$.

are taken from the literature [10, 116]. These interactions will in the following be termed “e-EAM” and are shown in figure 4.11. The extended EAM scheme (see equation 3.18) allows e.g. to reproduce the negative Cauchy pressure $P_\mathrm{C} = (C_{12} - C_{44})/2$ of Cr. However, the peculiar elastic properties of Cr already change, when about 5 at. % V is added [5]. Thus, simulations on NbCr$_2$ with the e-EAM interactions also probe if potentials fitted to properties of elemental metals give reasonable results for compounds.

4.2.2 Validation of the potentials

The fm-EAM potentials have been fitted to reproduce forces, total energies, and stresses. Thus, the evaluation of other properties already tests the validity and transferability of the interactions.

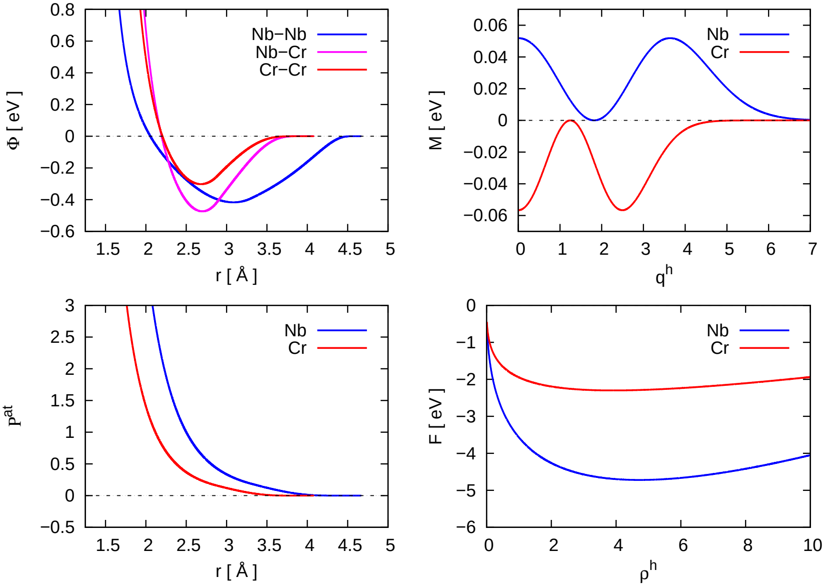

Figure 4.11: Analytical EAM potential functions for Nb-Nb, Cr-Cr, and Nb-Cr interactions [10, 116].

Lattice constant

The lattice constant a_{lattice} of NbCr$_2$ is derived by scaling the infinitely repeated unit cell, such that the pressure vanishes and the potential energy reaches its minimum. For the fm-EAM interactions a_{lattice} is 6.94 Å, the e-EAM potentials give 6.79 Å. Ab-initio calculations with VASP result in 6.97 Å. Calculations by Hong et al. [53] and Mayer et al. [79] yield values between 6.82 Å and 6.92 Å. The lattice parameter measured by experiment is 6.99 Å [105]. Thus, all values are very similar (see also table 4.1).

Elastic properties

The elastic constants are deduced from three independent lattice distortions as described in Hong et al. [53]. The obtained values are $C_{11} = 300$ GPa, $C_{12} = 181$ GPa, and $C_{44} = 55$ GPa for the fm-EAM potentials, whereas they are $C_{11} = 558$ GPa, $C_{12} = 259$ GPa, and $C_{44} = 102$ GPa for the e-EAM potentials. Thus, the values obtained for the e-EAM potentials are noticeably larger. The EAM values are compared with ab-initio and experimental data in table 4.1. The three ab-initio results presented there (columns VASP, Hong et al. [53], and Mayer et al. [79]) are in good agreement: C_{11} lies between 309 and 322 GPa, C_{12} between 185 and 216 GPa, and C_{44} between 69 and 83 GPa. The deviations can be assigned to different methods and approximations in the ab-initio calculations and the determinations of the elastic constants. A comparison to the values for the fm-EAM interactions indicates that the ab-initio data is resembled very well. If the VASP values are taken as reference, the fm-EAM results differ by about -3% for C_{11}, -9% for C_{12}, and -20% for C_{44}. The deviations between the different ab-initio calculations have the same order of magnitude. Thus, the fm-EAM potentials correctly describe the elastic constants, whereas the e-EAM potentials overestimate them (with VASP as reference: +81% (C_{11}), +31% (C_{12}), +48% (C_{44})). This behavior can be attributed to a limited transferability of the e-EAM potentials, which have been fitted to the elastic properties of the bcc elemental metals. The bulk, the Young's, and the shear moduli are calculated for all methods from the elastic constants and are shown together with experimental values in table 4.1. Obviously, experimental data confirm the calculations.

Elastic properties at large strains may also play a significant role for the simulation of fracture. To investigate this behavior we scale the coordinates of the atoms in [010] direction by $1 + \beta$. The positions are kept fixed and the stresses are calculated. So, a stress-strain relationship for the perfect crystal can be obtained. This procedure is rather artificial as the atoms would move and relax in a molecular dynamics simulation. However, it has been shown by Abraham [2] that e.g. the instability onset of brittle fracture is related to the secant modulus at the stability limit. Thus, the maximum stress and the corresponding strain should be represented well. In figure 4.12 the stress-strain behavior for the EAM potentials and for VASP calculations are shown. It is evident that the fm-EAM potentials reproduce the point of maximum stress well, whereas the e-EAM potentials underestimate it (see arrows in figure 4.12). For small strains it is again obvious that the e-EAM potentials overestimate the elastic constants. In contrary, the fm-EAM stresses coincide with the ab-initio values up to about 15% strain. How-

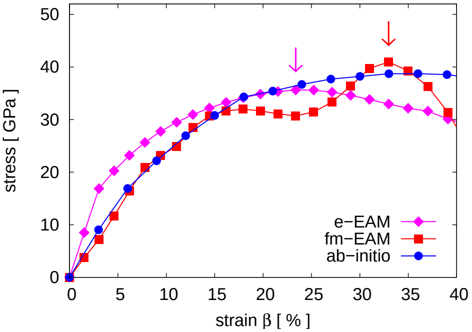

Figure 4.12: Stress-strain diagram [95].

ever, it is also apparent from the figure that the e-EAM potentials result in a smoother curve than the fm-EAM potentials. This is due to the fact that the atoms are not allowed to relax, due to the analytical expressions used for the e-EAM potentials, and due to their shorter interaction range. Increasing this range can help e.g. to distinguish systems with different stackings of layers (see section 1.2). Potentials with additional features in their long-range part also can help to stabilize structures. For example, the simple pairwise Dzugutov potential [28] is able to favor bcc [96] over close-packed structures like fcc. This is achieved by an additional maximum in the potentials at a larger distance. An advantage of the force-matching method is that one is able to define a reasonable interaction range. Potentials that are essentially zero after a certain distance may be truncated. The long-range part of the potentials, however, will also alter e.g. stress-strain curves. Thus, that these are a bit wavy for the fm-EAM potentials may be seen as a direct consequence of trying to describe accurately both equilibrium properties as well as the behavior at e.g. large strains or high temperatures.

Melting temperature

The fracture simulations are performed at low temperature (see section 3.2.5). However, the region close to the crack tip can get very hot. Thus, the melting temperature at vanishing pressure should not be too low. Determining T_{melt} with atomistic simulations may lead to some difficulties (see, e.g., [37, 62, 81]). If no free surfaces are present, the nucleation in the melting process is hindered. For monoatomic bulk Al it was reported [81] that the solid phase could be heated to temperatures 500 K above the melting temperature. Furthermore, NbCr$_2$ transforms from a C15 to a C14 structure (see, e.g., [105]) before melting at $k_{\mathrm{B}}T_{\mathrm{melt}} = 0.176$ eV (see table 4.1). It is questionable if EAM potentials are capable of describing this behavior satisfactorily. Anyway, the limited time scale of molecular dynamics simulations could impede the occurrence of such a transformation. By gradually and slowly increasing the temperature of a bulk sample in NPT-simulations, an upper bound for T_{melt} can be obtained. A distinct jump in the volume and in the mean square displacements indicates the melting of the sample. The obtained values (see table 4.1) seem reasonable for both e-EAM and fm-EAM potentials. However, the value for the e-EAM potential is already a bit too low (0.17 eV) and that for the fm-EAM potentials (0.24 eV) seems too high. The melting temperature can also be determined with the help of two-phase systems. There, a solid-liquid interface exists, so that some of the above mentioned problems can be circumvented. To evaluate the melting temperature of such a system, a periodically repeated cubic box is prepared. A central ball consists of the solid C15 Friauf-Laves phase and the rest is filled with the molten sample. Various NPT-simulations at constant temperatures near the melting temperature and at zero pressure are performed. If the central region totally melts, the temperature is above the melting temperature. The observation and simulation time has been limited to a maximum of 30 ns. The samples contain about 24 000 atoms. The obtained values for the melting temperature are given in table 4.1. With $k_{\mathrm{B}}T_{\mathrm{melt}} = 0.17$ eV the experimental data is resembled very well by the fm-EAM potentials, whereas the value for the e-EAM potentials (0.10 eV) is too low.

Free surfaces

A moving mode I crack generates free surfaces. Following Griffith (see section 2.2), potential cleavage planes should be those of low surface energy. To determine such planes for the EAM potentials, we relax a specimen and split it into two parts. Subsequently, the two regions are shifted rigidly apart. The mean surface energy $\bar{\gamma}$ of the two generated free surfaces then is calculated from the energy difference of the

Table 4.1: Results obtained for the fm-EAM and the e-EAM interactions, ab-initio and experimental data for bulk C15 $NbCr_2$ [95]. B is the bulk modulus. V and R denote Voigt and Reuss averages of Young's modulus E and the shear modulus G; Hill values are given where only one number appears.

	fm-EAM	e-EAM	VASP	Hong et al. [53]	Mayer et al. [79]	exp. [21, 105]
a_{lattice} [Å]	6.94	6.79	6.97	6.82	6.82 - 6.92	6.99
C_{11} [GPa]	300	558	309	316	316 - 322	
C_{12} [GPa]	181	259	198	216	185 - 216	
C_{44} [GPa]	55	102	69	71	69 - 83	
B [GPa]	221	359	235	249	229	229.4
$E_{\mathrm{V/R}}$ [GPa]	157/157	326/316	175/173	173/168	205	214.1
$G_{\mathrm{V/R}}$ [GPa]	57/57	121/117	64/63	62/61	76	79.6
$k_{\mathrm{B}}T_{\mathrm{melt}}$ [eV]	< 0.24	< 0.17				0.176
	0.17	0.10				

Table 4.2: Surface energies (in J/m^2) for the fm-EAM and the e-EAM potentials.

surface	fm-EAM unrelaxed / relaxed	e-EAM unrelaxed / relaxed
010	3.01 / 2.90	2.35 / 2.12
011	2.93 / 2.81	2.21 / 1.84
111	2.80 / 2.75 3.31 / 3.08	2.18 / 1.97 2.76 / 2.42

artificially cleaved and the undisturbed specimen. The corresponding results for (010), (011), and (111) surfaces are given in table 4.2. The calculations are repeated for free surfaces that are allowed to relax[9]. The "unrelaxed" surface energies for the e-EAM potentials lie between 2.18 and 2.76 J/m^2, the "relaxed" values range from 1.84 to 2.42 J/m^2. The fm-EAM potentials result in 2.80–3.31 J/m^2 for the unrelaxed case and give 2.75–3.08 J/m^2 for the relaxed case. Although the absolute values differ for the e-EAM and the fm-EAM interactions, there are common features as can be seen from figures 4.13 and 4.14. There, the unrelaxed surface energies are given for different cutting positions y (defined as in figures 3.1 and 3.2). As can be seen directly, $\bar{\gamma}$ does not depend on y for the (010) and (011) surfaces. In contrary, $\bar{\gamma}$ for the (111) surfaces takes two different values depending on y. The smaller value $\bar{\gamma}^{\mathrm{I}}_{111}$ is realized if the specimen is cut between a kagome and a triangular net (see section 1.2). For both EAM potentials the unrelaxed surface energies are ordered in the same way: $\bar{\gamma}^{\mathrm{I}}_{111} < \bar{\gamma}_{011} < \bar{\gamma}_{010} < \bar{\gamma}^{\mathrm{II}}_{111}$.

Ab-initio values of the surface energies have been computed in collaboration with Ali Al-Zu'bi. He performed his master's thesis[4] on this topic and was supervised by Prof. Dr. C. Elsässer. The calculations have been carried out with the mixed-basis pseudopotential code MBPP [31, 50, 77, 120] using the local density approximation (LDA). The lattice and elastic constants also have been evaluated (see table 4.3). These are in good agreement with the previous findings (see table 4.1). The values for the unrelaxed and relaxed surface energies are given in table

---

[9] The GLOK relaxator is used.

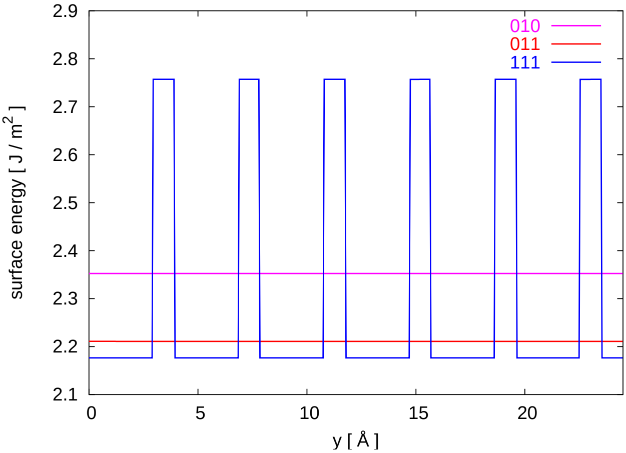

Figure 4.13: Surface energies (unrelaxed) for the e-EAM potentials.

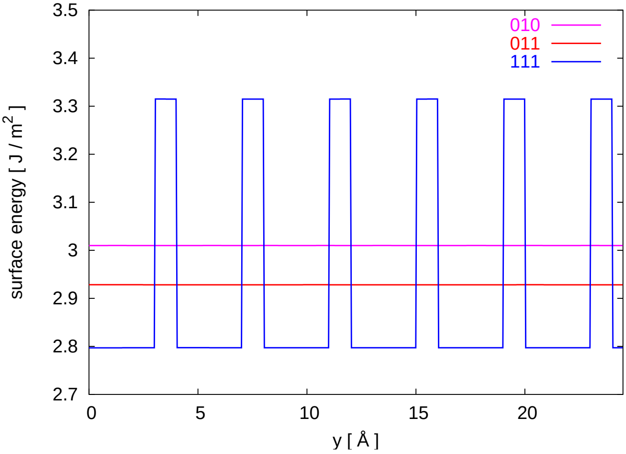

Figure 4.14: Surface energies (unrelaxed) for the fm-EAM potentials.

Table 4.3: Ab-initio results obtained by A. Al-Zu'bi [4] with the MBPP code.

a_{lattice} [Å]	6.85
C_{11} [GPa]	304
C_{12} [GPa]	218
C_{44} [GPa]	63

surface	surface energy [J/m^2] unrelaxed / relaxed
010	3.85 / 3.48
011	3.73 / 3.34
111	3.72 / 3.50

4.3. A comparison of these results to those of table 4.2 shows that both EAM potentials seem to underestimate the surface energies. Taking the ab-initio results as reference, the unrelaxed values for $\bar{\gamma}_{010}$, $\bar{\gamma}_{011}$, and $\bar{\gamma}^{\mathrm{I}}_{111}$ are smaller by 39%, 41%, and 41% for the e-EAM potentials and by 22%, 21%, and 25% for the fm-EAM potentials. The deviations for the relaxed case are -39%, -45%, and -44% for the e-EAM interactions and -17%, -16%, and -21% for the fm-EAM interactions. Studies on metals show that the use of the LDA can give about 10-20% larger surface energies than with the GGA [70, 111][10]. As such an uncertainty may already be applied to the ab-initio results, the estimates of the surface energies appear reasonable for both EAM potentials. However, the fm-EAM results again are closer to the ab-initio values.

Free surfaces should be stabilized in fracture simulations. Especially, no atoms should evaporate. This is not guaranteed for e.g. effective pair potentials which lack a deep first minimum. The relaxation behavior of a close-packed (111) surface is investigated in figure 4.15. Red and blue discs represent the initial positions of Cr and Nb atoms at the topmost layers. The yellow spots indicate their location after relaxation. Obviously, the surfaces are stabilized for the fm-EAM potentials (figure 4.15, left) and for the e-EAM potentials (figure 4.15, right). However, the atoms close to the surface behave differently. For the fm-EAM potentials the two top layers relax towards the bulk. Using the e-EAM potentials, the first layer of Nb atoms also moves inwards, but the next

---

[10] (010) surface energies calculated by Li et al. [75] (3.07 J/m^2) using the GGA are in excellent agreement with the results of the fm-EAM potentials (3.01 J/m^2) and lie below the values obtained with the MBPP code using the LDA (3.85 J/m^2).

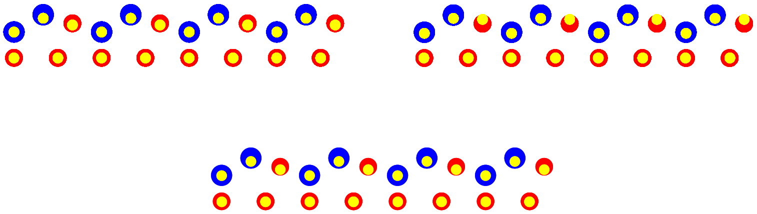

Figure 4.15: Relaxation of a (111) surface using fm-EAM potentials (left), e-EAM potentials (right), and ab-initio molecular dynamics (bottom) [95].

layer of Cr atoms moves away from the bulk. Ab-initio results obtained with VASP (figure 4.15, bottom) agree with the fm-EAM findings. The e-EAM interactions have been fitted to the properties of the elemental metals, e.g. the negative Cauchy pressure of bcc Cr. This may be the reason for the observed motion of the e-EAM Cr atoms at the surface of the simulated C15 compound (figure 4.15, right).

This difference in relaxation behavior may also influence crack propagation. $111_{2\bar{1}\bar{1}}$ (see abbreviation 3.32) fracture is investigated to test this effect. A seed crack of lowest surface energy $\bar{\gamma}^{\mathrm{I}}_{111}$ is inserted. The response of the system then is simulated as described in section 3.2.5. For the fm-EAM potentials the crack propagates in $[2\bar{1}\bar{1}]$ direction for $k \geq 1.2$ (see abbreviation 3.31). Brittle cleavage fracture with no indication of any dislocation activity is observed (see inset of figure 4.16). The crack moves up one atomic layer. This does not alter the surface energy, as cuts between $\alpha\, A$ or $A\, \alpha$ in the C15 stacking sequence (see section 1.2) require the same amount of energy. The surfaces of the fractured sample are geometrically scanned as described in section 3.2.5. A small square part with an edge length of about 5 nm is shown in figure 4.16. The kagome net (with a few defects) is clearly visible. The result of the same numerical experiment with the e-EAM potentials is also shown in figure 4.16. At first glance, the seed crack seems to emit a dislocation for $k = 1.1$. Cracks propagate only for very high loads (e.g. $k = 1.8$) and then leave rough fracture surfaces. The “ductile” manner of the

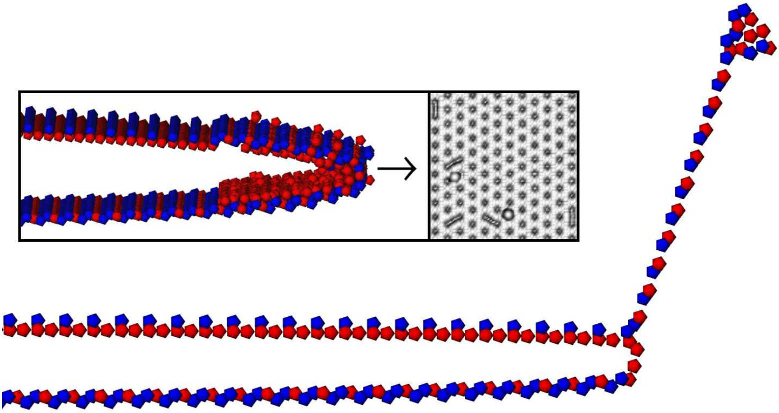

Figure 4.16: Atomic configurations near a $111_{2\bar{1}\bar{1}}$ crack tip using e-EAM and fm-EAM (inset) interactions [95].

e-EAM sample opposes the brittle behavior of the fm-EAM material. Experiments show that $NbCr_2$ is brittle up to about two-thirds of the melting temperature and fails by macroscopic fracture (see, e.g., [113]). Thus, the e-EAM potentials here yield questionable results. This indicates that EAM potentials fitted to properties of elemental metals can produce qualitatively wrong behavior when they are used for the interactions in intermetallic compounds.

Figure 4.17 shows atoms of the e-EAM sample near the faulted region. The initial configuration (left) resembles the C15 structure. The horizontal lines correspond to $(\bar{1}11)$ layers. The vertical lines help to identify the layer type. The stacking sequence (from bottom to top beginning with the first horizontal line) is given below the picture (see equation 1.2). After the loading (figure 4.17, right) the upper half of the region is shifted by $\mathbf{b} = a_{\text{lattice}}/6 \cdot [211]$ relatively to the lower half. This corresponds to a Shockley partial. However, the deformation is not caused by a simple dislocation or by synchro-shearing (see, e.g., [20]). The new stacking sequence indicates that layers have been exchanged in the

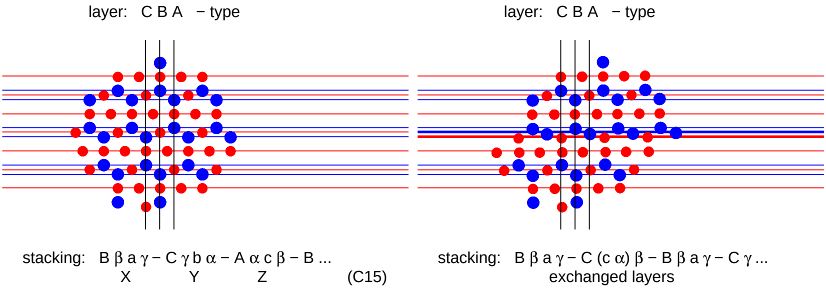
layer: C B A – type
layer: C B A – type
stacking: B β a γ – C γ b α – A α c β – B ...
X
Y
Z
(C15)
stacking: B β a γ – C (c α) β – B β a γ – C γ ...
exchanged layers

Figure 4.17: Stacking sequence before and after (see figure 4.16) the loading of a crack using e-EAM potentials [95].

middle of the configuration. Only the atoms in these layers lose their usual coordination. Thus, two layers of atoms mark the fault in figure 4.16. This leads to a stacking sequence $(c\alpha)\beta$ that cannot be found in any Friauf-Laves phase (compare to equations 1.1, 1.2, and 1.3). Such a relative movement of atomic layers has also been observed at the free surface (see figure 4.15, right). Therefore, this defect mechanism can be regarded as an artefact caused by the e-EAM potentials.

Concluding this section 4.2.2, it has been shown that the fm-EAM potentials resemble well ab-initio and experimental data. These interactions outperform available (e-EAM) potentials when properties of the intermetallic compound $NbCr_2$ are investigated. The reliability allows for a systematic study on crack propagation in this compound.

4.2.3 Fracture simulations

Crack propagation in $NbCr_2$ is studied in detail in this section. The fm-EAM potentials are used in the numerical simulations as they have proven to give reasonable results (see section 4.2.2). The system is prepared and visualized as described in section 3.2.5. Diverse loads are applied to differently oriented samples. The results are then analyzed and discussed.

Orientations

The investigated orientations are displayed in figure 4.18. The crack propagation direction x and an axis y perpendicular to the cleavage plane are given by the notation y_x (see abbreviation 3.32). A cubic cell in the corresponding arrangement is projected onto the xy-plane (figure 4.18, left). Slightly tilted samples are also depicted (figure 4.18, right) to show how the atoms are arranged in the z-direction. The chosen cleavage plane is indicated by a line and a pair of scissors. A cut that gives the lowest surface energy $\bar{\gamma}^{\mathrm{I}}_{111}$ is chosen in the cases where y is a [111] direction. For the other samples, the surface energy does not depend on the y-position of the plane (see figure 4.14). This is directly evident from the 011_{100} sample (figure 4.18, left). However, the 010_{101} orientation reveals that for different y-positions atoms are not approached in the same way by the crack. The projection of a slightly deformed prolate rhombohedron (see section 1.2) is indicated in figure 4.18. Obviously, one can cut the highlighted 010_{101} rhombohedron with or without separating the two blue spheres.

Velocities

Figures 4.19, 4.20, 4.21, and 4.22 show the position of the crack tip versus time. The applied load is characterized by the reduced stress intensity factor k (see abbreviation 3.31) and is varied up to $k = 1.8$. Thus, the energy release rate would in principle be sufficient to generate surfaces that require up to $k^2 = 3.24$ times the energy of the flat seed crack. As is evident from the figures, loads above the Griffith value ($k = 1$) are needed for crack propagation. The seed crack moves at least several nanometers for $k \geq 1.2$. Crack motion at a lower value of $k = 1.1$ is only observed for the $111_{0\bar{1}1}$ sample. So, the lattice trapping effect (see section 2.4) causes initial energy release rates that exceed the Griffith value by about 20 to 40%. This surplus of energy can cause radiation and rough fracture surfaces.

- Figure 4.19 shows that the 010_{101} crack moves at steady state for $k > 1.1$. Small fluctuations of the velocity are visible for $k = 1.2$ and $k = 1.3$. The average crack velocities (dashed lines in figure 4.19) increase with increasing load.
- The same statements are true for the 011_{100} sample (see figure 4.20). However, for $k = 1.2$ the crack is arrested after about 15

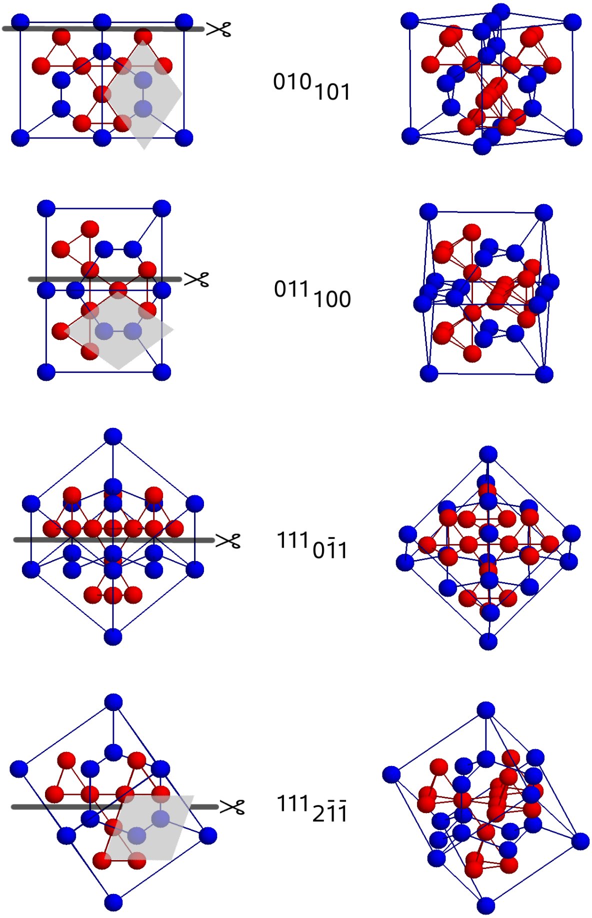
010 101
011 100
111 01̄1
111 21̄1̄

Figure 4.18: Orientations of the samples.

ps. The fluctuations around the mean velocity for $k = 1.3$ are larger than for the 010_{101} crack.

- A similar behavior is also observed for the orientation $111_{0\bar{1}1}$ (see figure 4.21). It is only shifted to lower k values. Crack arrest is observed after about 25 ps for $k = 1.1$. For $k = 1.2$ a steady state velocity cannot be defined.
- The $111_{2\bar{1}\bar{1}}$ seed cracks achieve already a high mean velocity at low loads (see figure 4.22). At the onset of fracture, the cracks seem to accelerate for $k \leq 1.3$.

The average crack velocities v for the diverse loads and orientations are summarized in figure 4.23. The speed increases with increasing k. The cruxes indicate that only a selected part of the data has been included in the fit of v. The marked $111_{0\bar{1}1}$ and 011_{100} cracks are arrested after a certain time. Only data before this incident is used to obtain v (see figures 4.21 and 4.20). In contrary, only data after the initial acceleration time is chosen for the $111_{2\bar{1}\bar{1}}$ cracks tagged in figure 4.23 (see figure 4.22).

The measured velocities lie in a range of about 0.4 $\frac{\mathrm{km}}{\mathrm{s}}$ to 1.5 $\frac{\mathrm{km}}{\mathrm{s}}$. Anderson [9] defined an average transverse sound velocity $\bar{v}_\mathrm{t}$,

$$\bar{v}_\mathrm{t} = \sqrt{\frac{G_\mathrm{R} + G_\mathrm{V}}{2\rho}},$$

where ρ is the density. The elastic and lattice constants of table 4.1 for the fm-EAM potentials together with the atomic masses of the chemical elements yield $\bar{v}_\mathrm{t} \approx 2.7\frac{\mathrm{km}}{\mathrm{s}}$. Thus, the observed crack velocities are in a range of about 15-56% of $\bar{v}_\mathrm{t}$.

A minimal non-zero value of the crack velocity (a velocity gap) is often observed in molecular dynamics simulations. According to Marder [78] it is a consequence of rapidly snapping bonds. If crack propagation becomes too slow, too much energy is dispersed from the crack tip by phonons before the crack arrives at the next bond. At a critical velocity, this bond will not break. The maximal observed velocity lies below the Yoffe value $v_\mathrm{Y} \approx 0.6 v_\mathrm{t}$ (see section 2.3). A maximal crack velocity $v_\mathrm{max} = v_\mathrm{Rayleigh} \approx v_\mathrm{t}$ was proposed by Stroh [104], as a crack

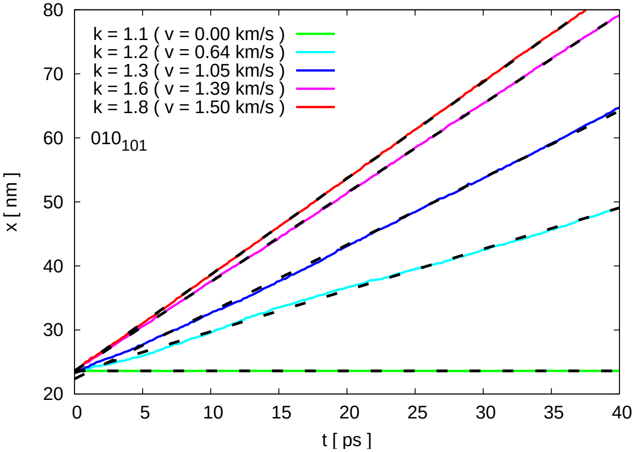

Figure 4.19: Crack-tip position vs. time for the orientation 010_{101}.

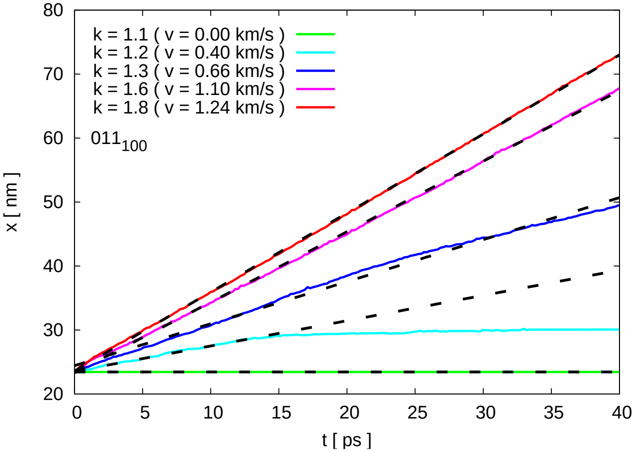

Figure 4.20: Crack-tip position vs. time for the orientation 011_{100}.

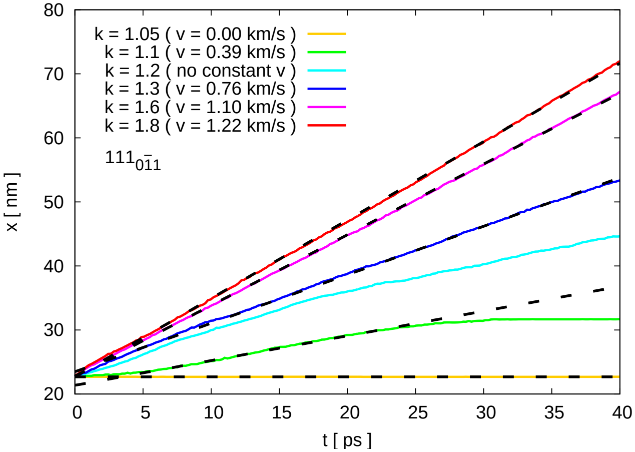

Figure 4.21: Crack-tip position vs. time for the orientation $111_{0\bar{1}1}$.

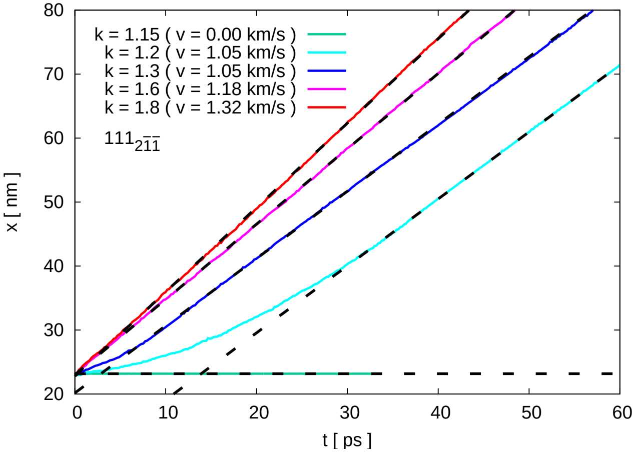

Figure 4.22: Crack-tip position vs. time for the orientation $111_{2\bar{1}\bar{1}}$.

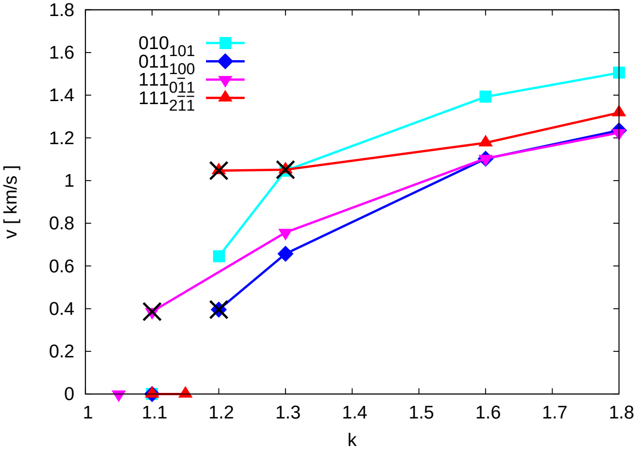

Figure 4.23: Crack velocities.

resembles a strong deformation of a free surface. Thus, the velocity range obtained by the simulations is reasonable. Further knowledge is needed to understand details of the orientation dependence of crack propagation. For this purpose, the fracture surfaces are investigated in the next section.

Fracture surfaces

The fracture surfaces of the samples are geometrically scanned as described in section 3.2.5. The height h_0 of the seed crack is encoded in green. Regions in blue lie at least 5Å below this initial level. The color red is used to represent values $h \geq h_0 + 5$Å. Large red areas indicate that the crack has not propagated through this region within the simulation time. A surface is denoted “upper” (“lower”) fracture surface, if the y-position of the corresponding atoms is higher (lower) than the crack height (see, e.g., figure 3.2). The roughness and surface energy of the upper and lower surfaces may differ, as these can be formed by different atomic species in various arrangements. Thus, both surfaces are displayed. For this purpose, the upper part of the specimen is rotated by 180° around the x-axis and scanned. So, red areas in the lower fracture surface should give rise to blue areas in the upper fracture surfaces, and so on. Color-coded sections of lower (upper) fracture surfaces are given in figures 4.24, 4.26, 4.28, and 4.30 (4.25, 4.27, 4.29, and 4.31) for the orientations 010_{101}, 011_{100}, $111_{0\bar{1}1}$, and $111_{2\bar{1}\bar{1}}$.

- The lower fracture surfaces of the 010_{101} sample are displayed for $k = 1.2$, $k = 1.3$, and $k = 1.6$ in figure 4.24. The corresponding upper fracture surfaces are given in figure 4.25. The surfaces are rough on an atomic scale. Yellow areas on the lower surfaces and turquoise features on the upper surfaces indicate that the crack has moved up about one atomic layer from its initial position.

- The 011_{100} crack stops moving after several nanometers (see figure 4.20) for $k = 1.2$. From figures 4.26 and 4.27 one might conclude that an increased roughness hinders further crack advance. For higher k values, there are larger regions where atoms of other layers appear. There is no clear tendency for the crack height. For $k = 1.3$ it increases on average (due to yellow regions in figure 4.26, middle), for $k = 1.6$ it decreases (due to turquoise regions in figure 4.26, bottom). However, the resulting structures on these surfaces look quite similar (compare figure 4.26 (middle) with figure 4.27 (bottom)).

- The propagating $111_{0\bar{1}1}$ crack is arrested for $k = 1.1$ (see figure 4.21). The resulting fracture surface seems to be flat apart from some point defects (see figures 4.28 (top) and 4.29 (top)). At higher loads, the fracture surfaces are formed by atoms of the initial and the subsequent layer.

- The crack in the $111_{2\bar{1}\bar{1}}$ specimen moves up one atomic layer and stays on this height. Perfect brittle cleavage fracture is observed. Some point defects are present for $k = 1.2$. The defects and the roughness increase for $k = 1.3$ and $k = 1.6$ (see figures 4.30 and 4.31). One has to note here the dissimilarity of the $111_{2\bar{1}\bar{1}}$ and the $111_{0\bar{1}1}$ surfaces. The different in-plane crack propagation directions seem to strongly influence fracture behavior.

There are similarities to the results of the fracture simulations with the Lennard-Jones model interactions (see section 4.1.2). The fracture surfaces are rough on an atomic scale. Propagating $111_{2\bar{1}\bar{1}}$ cracks result in smooth fracture surfaces. The surfaces of the other orientations are rougher. However, the 011_{100} and 010_{101} cracks do not result in perfectly periodic patterns as shown in figures 4.7 and 4.8 (right). As the EAM interactions include many-body terms, these could give rise to a more pronounced roughness. But the higher lattice trapping (crack propagation is initiated at higher k values) of the EAM potentials for $NbCr_2$ has also be taken into account. The 010_{101} surfaces at a comparable load again look similar, as can be seen from a comparison of figure 4.24 (middle) and figure 4.8 (left) at $k = 1.3$. So, the results of the model potentials qualitatively resemble those of the material specific interactions.

The peak-to-valley roughness and the root-mean-square roughness of the fracture surfaces of figures 4.24 – 4.31 are given in figures 4.32 and 4.33. The values of the lower (upper) surfaces are marked by triangles pointing downwards (upwards). The initial flat cuts have the lowest unevenness. The roughness seems to increase with increasing load. This tendency is violated for the propagating 010_{101} and 011_{100} cracks at the lowest loads. The $111_{2\bar{1}\bar{1}}$ fracture surfaces are those of lowest roughness for low loads, as is already obvious from visual inspection of figures 4.24 – 4.31. The upper surfaces of the $111_{2\bar{1}\bar{1}}$ crack are rougher (see red lines in figure 4.33) than the lower ones. This is in contrast to the planes of the initial seed crack. Thus, the role of the upper and the role of the lower fracture surface seem to interchange.

All the samples have also been relaxed at $k = 1.3$ with the GLOK algorithm (see section 3.2.4). The corresponding results are given in figure 4.34. No remarkable differences to the previous surfaces (see figures 4.24, 4.28, and 4.30, middle) are obvious for the orientations 010_{101} (figure 4.34, top left), $111_{0\bar{1}1}$ (figure 4.34, top right), and $111_{2\bar{1}\bar{1}}$ (figure 4.34, bottom right). In the 011_{100} case (figure 4.34, bottom left) the crack climbed about one atomic layer. This is not observed for the propagating crack in figure 4.26, middle. However, it has already been pointed out that there is no clear tendency for the crack height in this sample for different k values. So, ignoring the height, the patterns again look similar. Thus, one might conclude that the dynamics of the system does not influence the resulting fracture surfaces very much.

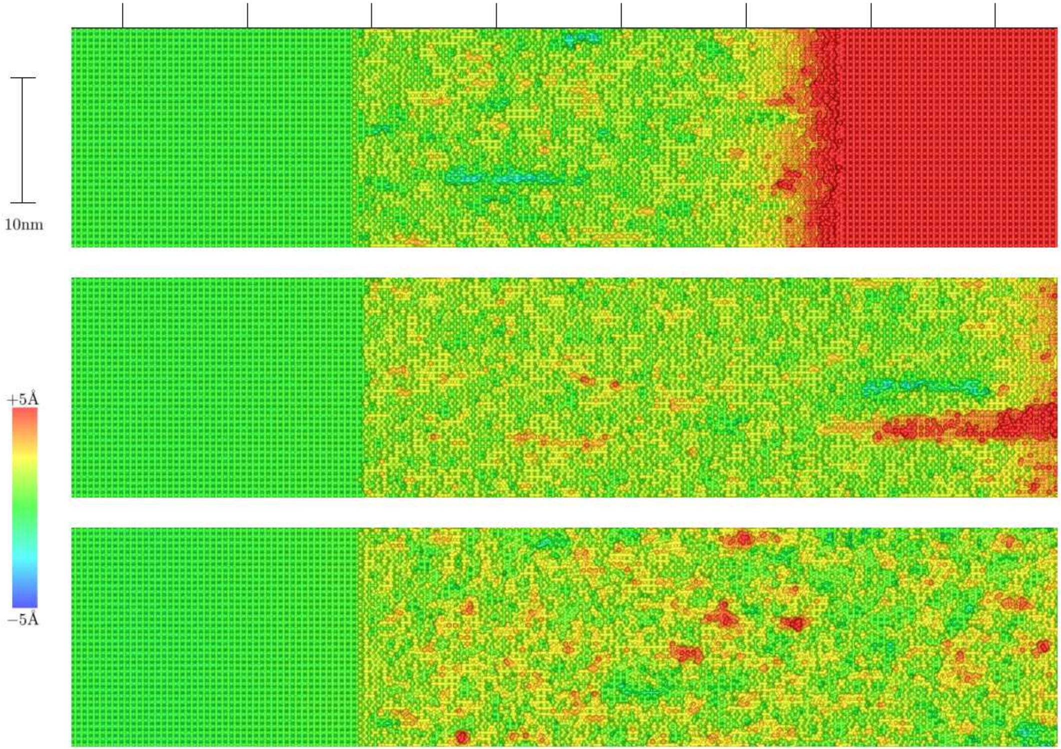

Figure 4.24: Lower 010_{101} fracture surfaces, loads: $k = 1.2$ (top), $k = 1.3$ (middle), and $k = 1.6$ (bottom).

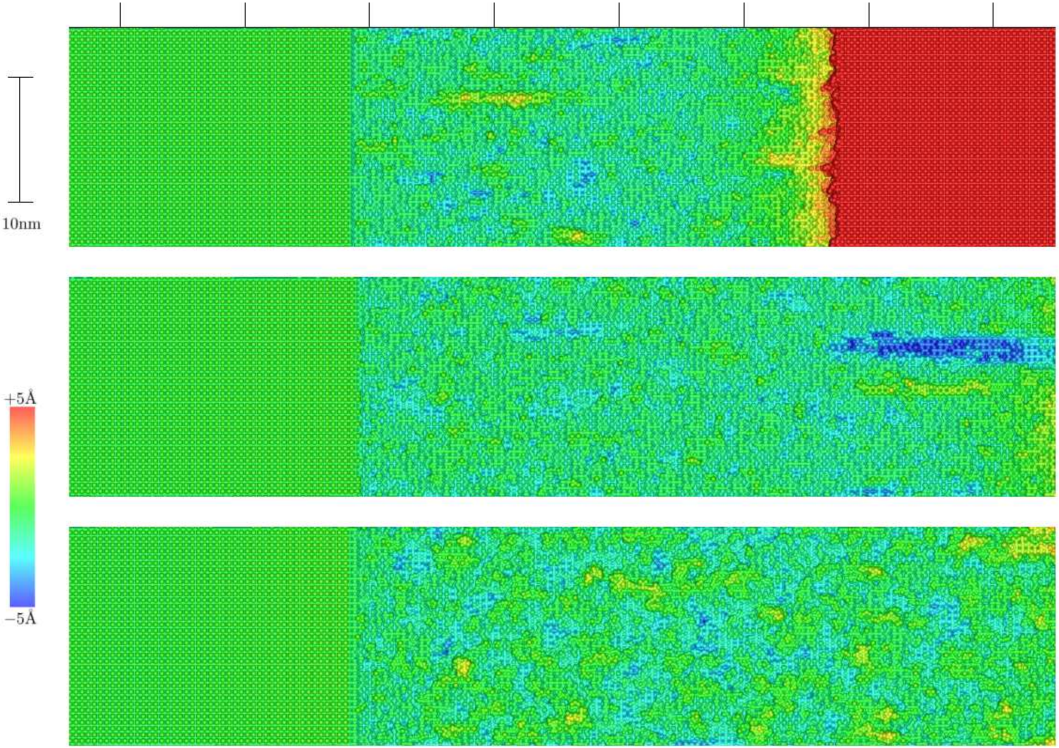

Figure 4.25: Upper 010_{101} fracture surfaces, loads: $k = 1.2$ (top), $k = 1.3$ (middle), and $k = 1.6$ (bottom).

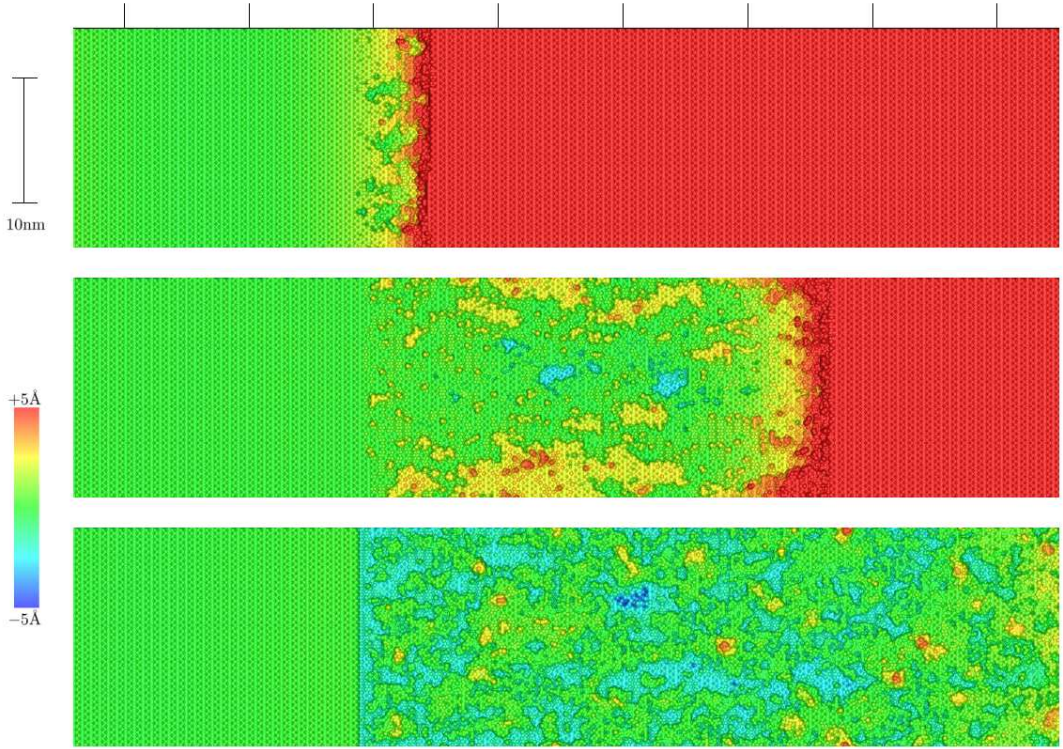

Figure 4.26: Lower 011_{100} fracture surfaces, loads: $k = 1.2$ (top), $k = 1.3$ (middle), and $k = 1.6$ (bottom).

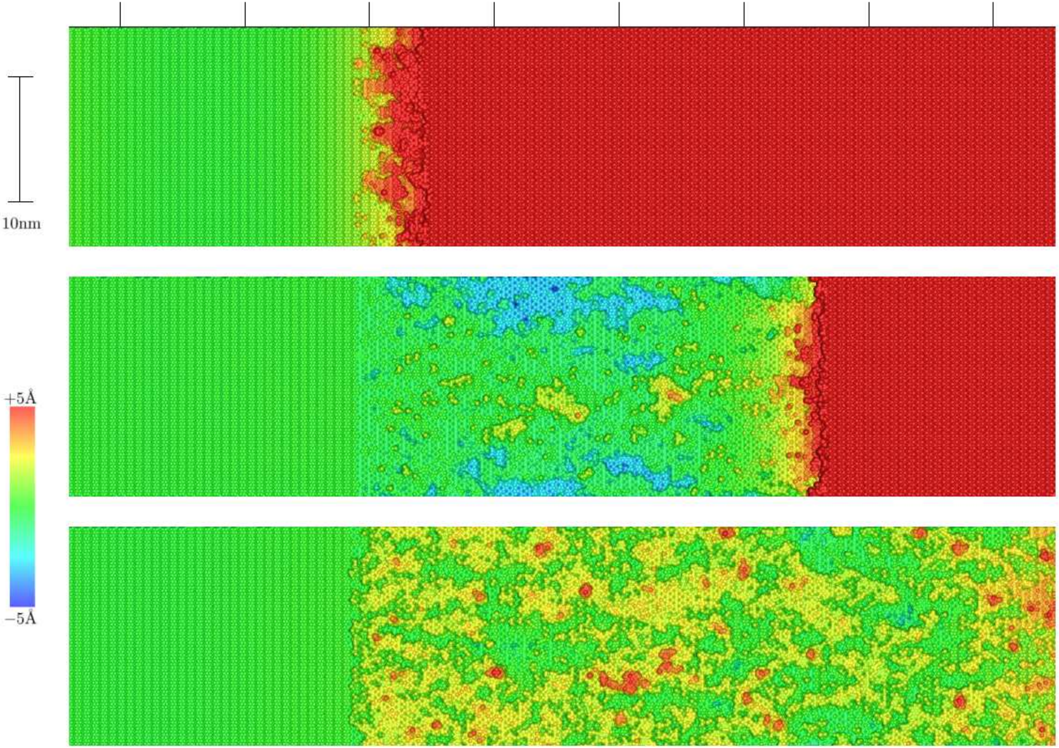

Figure 4.27: Upper 011_{100} fracture surfaces, loads: $k = 1.2$ (top), $k = 1.3$ (middle), and $k = 1.6$ (bottom).

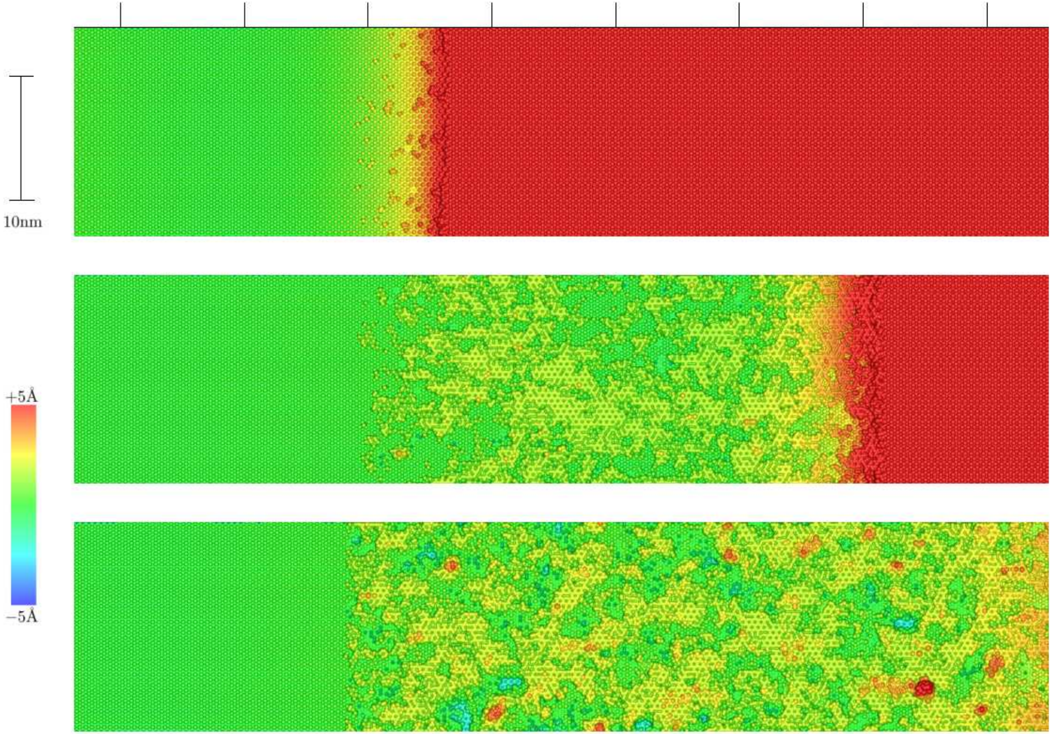

Figure 4.28: Lower $111_{0\bar{1}1}$ fracture surfaces, loads: $k = 1.1$ (top), $k = 1.3$ (middle), and $k = 1.6$ (bottom).

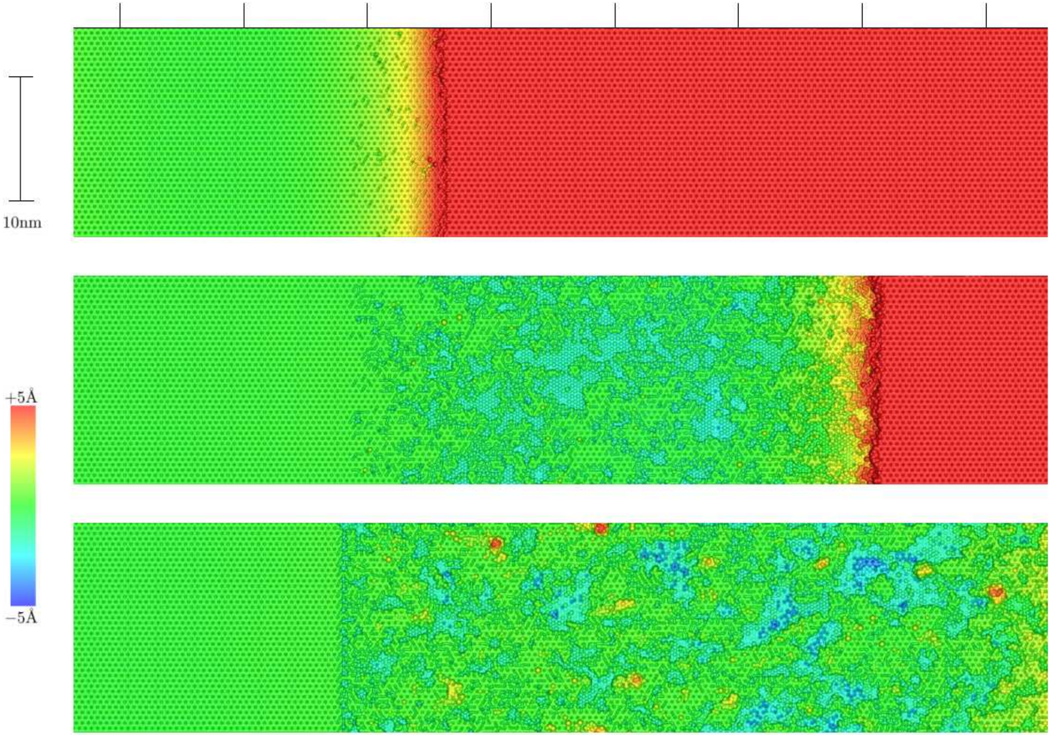

Figure 4.29: Upper $111_{0\bar{1}1}$ fracture surfaces, loads: $k = 1.1$ (top), $k = 1.3$ (middle), and $k = 1.6$ (bottom).

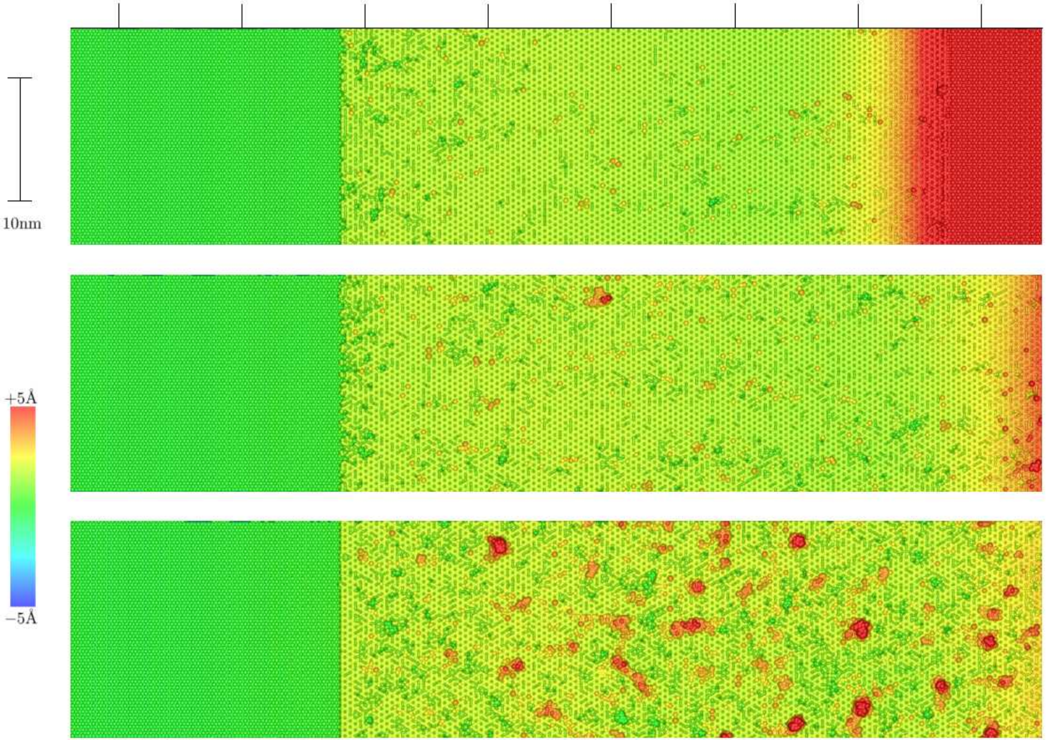

Figure 4.30: Lower $111_{2\bar{1}\bar{1}}$ fracture surfaces, loads: $k = 1.2$ (top), $k = 1.3$ (middle), and $k = 1.6$ (bottom).

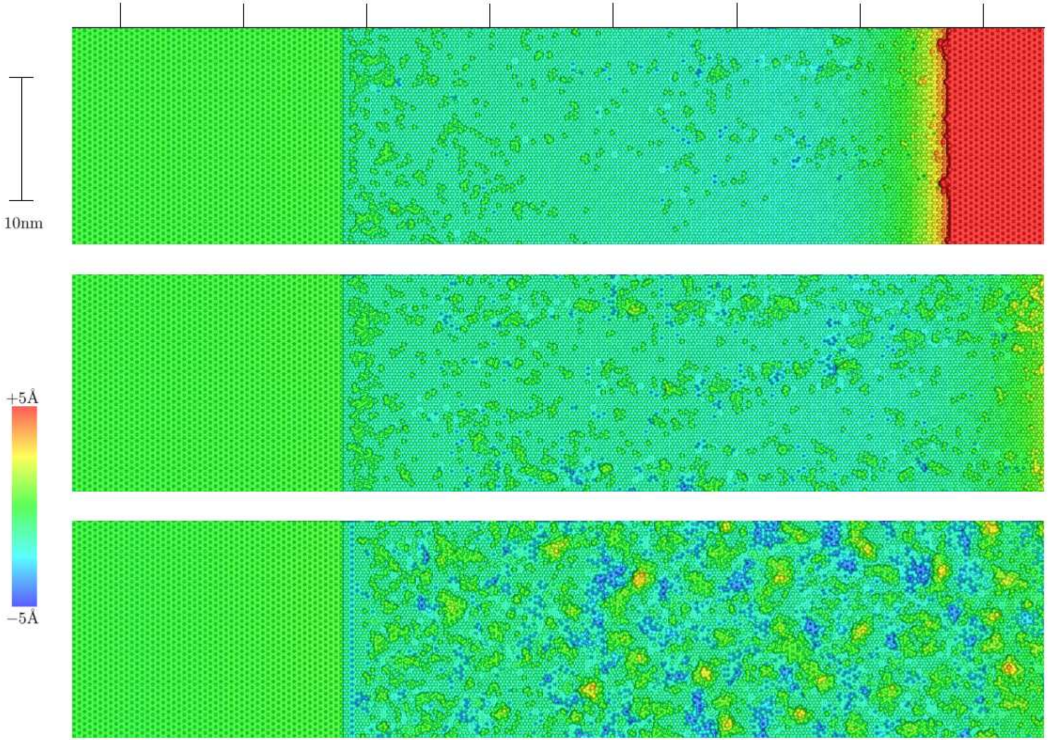

Figure 4.31: Upper $111_{2\bar{1}\bar{1}}$ fracture surfaces, loads: $k = 1.2$ (top), $k = 1.3$ (middle), and $k = 1.6$ (bottom).

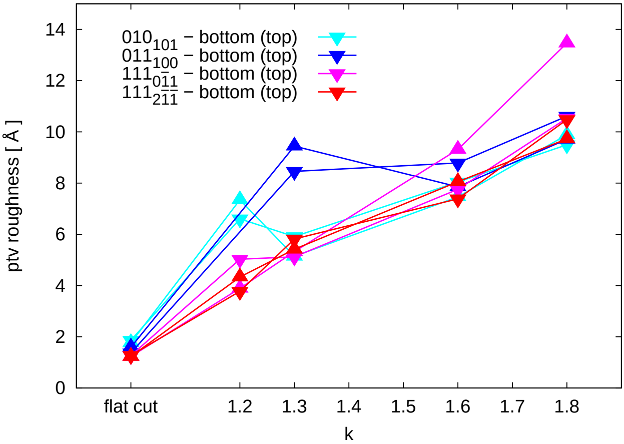

Figure 4.32: Peak-to-valley (ptv) roughness of the fracture surfaces.

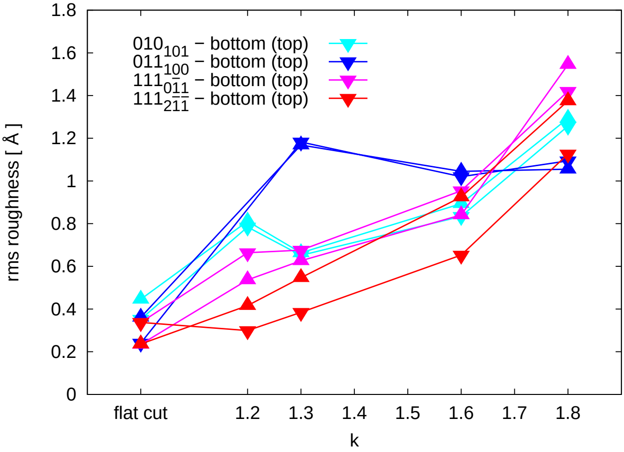

Figure 4.33: Root-mean-square (rms) roughness of the fracture surfaces.

Shifted seed cracks

Yellow areas in figures 4.24, 4.28, and 4.30 indicate that the cracks systematically deviate upwards from the initial layer. To further test this behavior, the initial seed cracks are shifted up one atomic layer. The corresponding surfaces for $k = 1.2$ are shown in figure 4.35. The fractured 010_{101} (left), $111_{0\bar{1}1}$ (middle), and $111_{2\bar{1}\bar{1}}$ (right) samples are very similar to the ones with the unshifted seed crack. Green regions in the images indicate that the crack stays on the new initial level.

- In the 010_{101} case, the mean surface level (see figure 4.35, left) does not deviate much from the primary height. Crack propagation and the final fracture surfaces seem not to be influenced by the height of the seed crack.
- Turquoise features in the $111_{0\bar{1}1}$ surface (see figure 4.35, middle) show that the crack fluctuates around the kagome layer. There are no obvious differences to the unshifted case.
- The $111_{2\bar{1}\bar{1}}$ seed crack results in nearly perfect brittle cleavage (see figure 4.35 (right) and figure 4.36). Thus, the (111) fracture surfaces for different propagation directions disagree as before. The shift of the seed crack gives a smaller lattice trapping, as the initial change of the layer is omitted. Propagation already is possible at $k = 1.1$ (see figure 4.37) instead of $k = 1.2$ (see figure 4.22).

Summarizing, the y position of the seed crack also does not significantly change fracture behavior. The characteristics of the fracture surfaces stay the same.

Energy considerations

The samples of figures 4.24 – 4.31 now are investigated from an energy viewpoint. The atoms forming the upper and lower part of the fractured sample are taken back to their positions in the relaxed initial sample. The two parts are then shifted apart rigidly. The surface energy now is calculated from the energy difference of these two specimens. In figure 4.38 the values of the upper (triangles pointing upwards) and lower (triangles pointing downwards) surfaces, as well as the averages (discs) are displayed in red color for $k = 1.3$. At this load it is possible for all

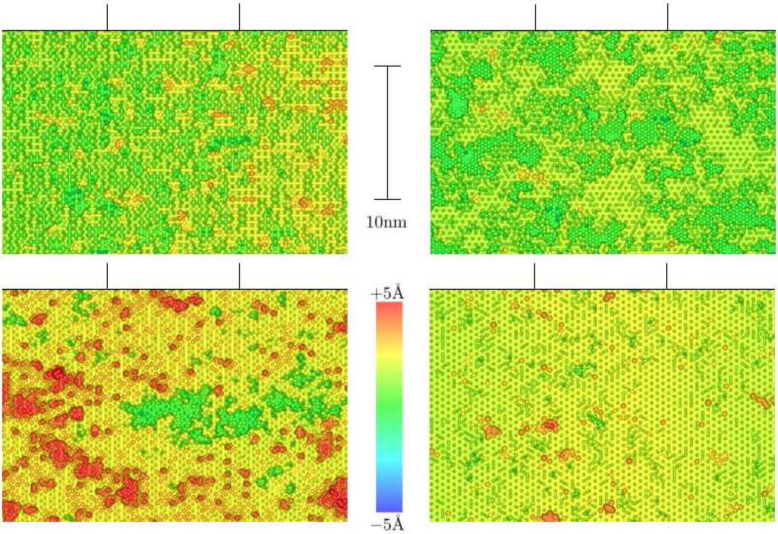

Figure 4.34: Surfaces obtained with the GLOK relaxator ($k = 1.3$).

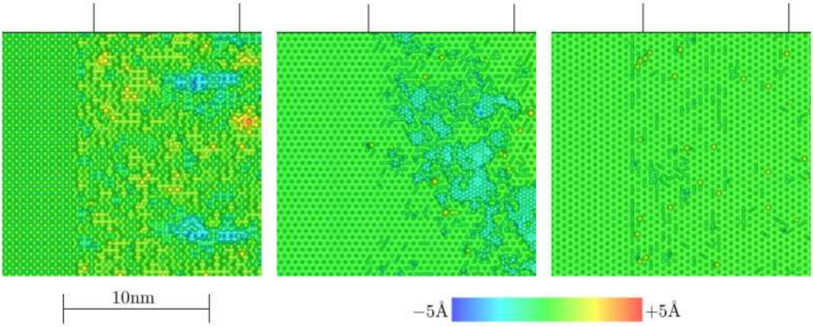

Figure 4.35: Sections of fracture surfaces caused by the shifted seed cracks, $k = 1.2$.

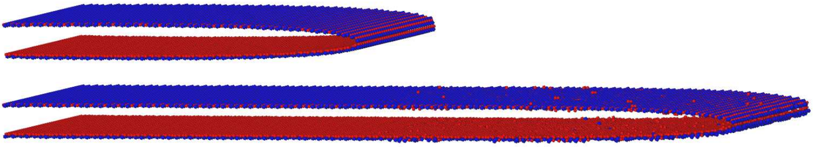

Figure 4.36: Atoms forming the fracture surfaces for the orientation $111_{2\bar{1}\bar{1}}$, $k = 1.15$, and the shifted seed crack. Top: $t = 0$, bottom: $t = 102\,\text{ps}$.

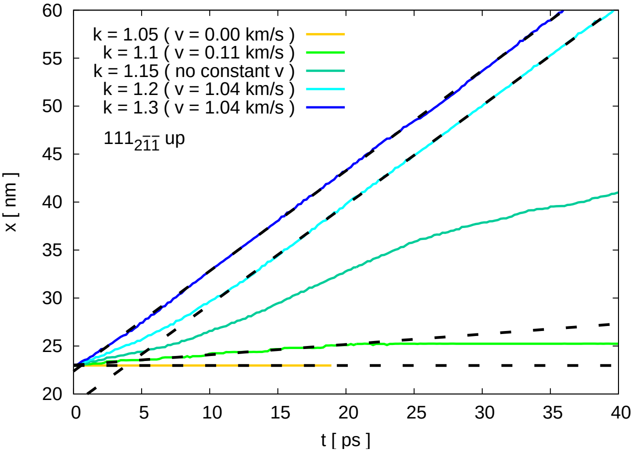

Figure 4.37: Crack-tip position vs. time for the orientation $111_{2\bar{1}\bar{1}}$ and the shifted seed crack (compare to figure 4.22).

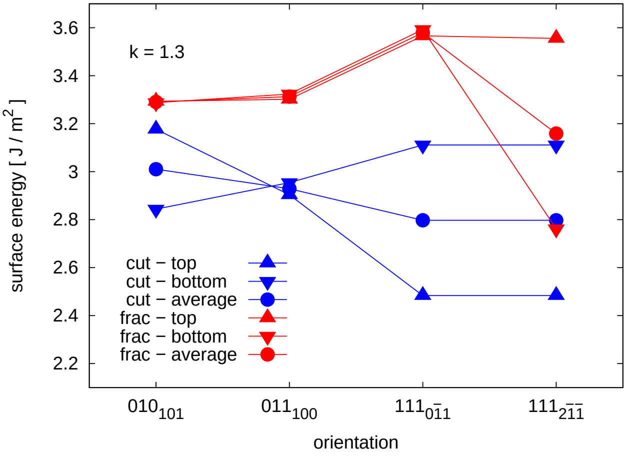

Figure 4.38: Surface energies.

cracks to overcome the lattice-trapped state and to move at constant velocity (see figures 4.19 – 4.22). The corresponding surface energies for flat cuts are given in blue in figure 4.38. The values $\bar{\gamma}$ represented by the blue circles have already been calculated in section 4.2.2. In this section, it has also been pointed out that $\bar{\gamma}$ for the (010) and (011) surfaces does not depend on the height y of the cut. In contrast, $\bar{\gamma}$ does depend on y for the (111) surfaces (see figure 4.14). The minimal value has been chosen for the initial seed cracks in the $111_{0\bar{1}1}$ and $111_{2\bar{1}\bar{1}}$ samples. However, this value is also realized for a crack that is shifted up one atomic layer. This corresponds to cuts between e.g. $\alpha\, A$ or $A\, \alpha$ in the C15 stacking sequence (see section 1.2 and figure 4.18).

It is evident from figure 4.38 (blue symbols) that the upper surface energy of the flat cuts differs significantly from the lower one for the 010_{101}, $111_{0\bar{1}1}$, and $111_{2\bar{1}\bar{1}}$ samples. This is not the case for the 011_{100} orientation. Of course, the values for the flat cuts have to be the same for the $111_{0\bar{1}1}$ and the $111_{2\bar{1}\bar{1}}$ specimen. They only differ by the crack propagation direction. The average surface energies of the fractured samples $\bar{\gamma}_{\text{frac}}$ (red discs) always lie above those of the seed cracks $\bar{\gamma}_{\text{cut}}$

(blue discs). Some of the energy surplus – which is needed to overcome the lattice-trapping – obviously causes surfaces of higher energy. The biggest raise is observed for the $111_{0\bar{1}1}$ case (see figure 4.38), where $\bar{\gamma}_{\mathrm{frac}} \approx 1.28\bar{\gamma}_{\mathrm{cut}}$[11]. For $k = 1.3$ the energy release rate is increased to about 169% of the Griffith value. Thus, most of the energy surplus always goes into radiation. For the orientations 010_{101}, 011_{100}, and $111_{0\bar{1}1}$ the energy of the upper surface equals the energy of the lower surface in the fractured samples (red triangles in figure 4.38). These energies only differ for the $111_{2\bar{1}\bar{1}}$ case, where nearly perfect cleavage occurs on an atomic plane. Thus, when a roughening of the surface occurs, the crack seems to choose a path that tends to generate upper and lower surfaces of the same energy. Due to defects (see figure 4.30, middle), $\bar{\gamma}$ is also higher in the $111_{2\bar{1}\bar{1}}$ fractured sample ($\bar{\gamma}_{\mathrm{frac}} \approx 1.13\,\bar{\gamma}_{\mathrm{cut}}$). A switching order of the triangles in figure 4.38 indicates (as in the case of the roughness) that the roles of the upper and of the lower surface have interchanged (a cut between $\alpha\,A$ leads to fracture between $A\,\alpha$, as mentioned above).

Atomistic aspects

The previous results demonstrate that it is possible to derive quantitative macroscopic data from atomistic fracture simulations. It has also been shown that the crack propagation direction within the same cleavage plane can affect this data. Crack velocities and fracture surfaces significantly differ for the $111_{0\bar{1}1}$ and the $111_{2\bar{1}\bar{1}}$ samples. Pure global energy considerations are not able to predict this. So, the simulations further indicate that investigations on an atomic scale are necessary to fully capture fracture behavior. To motivate the relevance of the discrete nature of matter, the local energy cost for $111_{2\bar{1}\bar{1}}$ cleavage is displayed in figure 4.39. The radius of the discs is proportional to the energy needed for a local increase of the cleavage planes. Expressed in an oversimplified picture, the figure shows, how much energy is required to snap the bonds between the atoms (see section 2.4). A vertical line represents a straight $111_{2\bar{1}\bar{1}}$ crack front in figure 4.39, a horizontal line a $111_{0\bar{1}1}$ crack front. Two such lines with the same length are indicated in figure 4.39. Obviously, the maximum number of large discs per crack

---

[11] If a similar increase of $\bar{\gamma}_{\mathrm{frac}}$ is assumed for $k = 1.1$, then the surplus of 21% in elastic energy might not be sufficient for the fracture of the whole sample. Indeed, crack arrest is observed in this case (see figure 4.21).

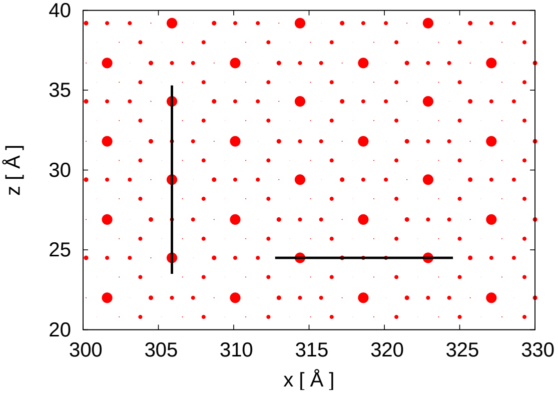

Figure 4.39: Local energy cost for $111_{2\bar{1}\bar{1}}$ cleavage.

length differs for the two propagation directions. Hence, a different lattice trapping and fracture behavior of the two orientations is reasonable and understandable.

Summary

In this thesis, the fracture behavior of complex metallic alloys at low temperature has been simulated by atomistic molecular dynamics simulations.

In simplified model systems, the influence of the structure on crack propagation has been studied. An icosahedral quasicrystal and a C15 Friauf-Laves phase with Lennard-Jones interactions indicate that the basic building blocks of the structures strongly influence fracture behavior. The clusters in the quasicrystal play a comparable role to the atoms in the Friauf-Laves phase as they affect the overall roughness of the fracture surfaces. It has been shown that crack propagation is strongly influenced by the local arrangement of atoms or clusters close to the crack tip.

To gain material specific information on C15 $NbCr_2$, interactions have been matched to ab-initio data. The corresponding potentials reproduce well physical properties related to fracture. Crack propagation has been investigated in differently oriented samples under diverse applied loads. Cracks propagate only for loads above the Griffith criterion due to the lattice-trapping effect. So, the fracture surfaces are not implicitly those of lowest energy or lowest roughness. However, most of the surplus of energy causes radiation. Brittle fracture is observed for all orientations. The roughness and energy of the fracture surfaces as well as the path and speed of the cracks do not only depend on the cleavage plane but also on the crack propagation direction. This reveals the influence of the atomistic nature of matter. The number, strength, and orientation of "bonds" approached by a crack define whether, where, and how it propagates.

Summarizing, it has been shown that it is possible to derive qualitative and quantitative information on crack propagation in intermetallic alloys by numerical experiments. Detailed analyses of the simulations highlight that processes on the atomic level determine fracture behavior.

Appendix

Height-height correlation function

Quasicrystals are composed of atomic clusters (see section 1.1). It is an ongoing and persistent discussion, whether these geometric building blocks also represent physical entities. Experiment and simulation show that cleavage surfaces of icosahedral quasicrystals are rough with cluster-like protrusions (see section 4.1.1). However, by sputtering and annealing at high temperatures, nearly flat surfaces can be produced. So, obviously, the clusters cannot be termed supermolecules. At first glance, recent findings also seem to deny a physical role of the clusters in the fracture process. Ponson et al. [86] measured the roughness exponent of experimental fracture surfaces and questioned a signature of clusters. In this appendix, it is shown that the results of Ponson et al. cannot negate the role of the clusters in the fracture process.

A method to study the roughness of fracture surfaces is to calculate the height-height correlation functions. These uncover scaling properties with a “universal” roughness exponent of about 0.8 for a wide range of materials [15]. However, so far, no theoretical model is able to satisfactorily comprise this self-affinity. So, it seems to be impossible to interpret microscopic properties of the investigated structures starting from the scaling behavior. It is even hard to distinguish a fractured from a sputtered surface, as the roughness exponents of both surfaces can lie in the same range. Although the scaling properties of cracks seems to be “universal”, the range of length scales in which this universality is valid strongly varies for different materials. It has been proposed that the associated cutoff length ξ is related to the size of the process zone R_c[13]. Inside this area, linear elastic predictions deviate from the real deformation field. Such a nonlinear and dissipative region always has to exist, as atomic bonds break at the crack tip. The behavior on and below this scale defines whether, how, and where a crack propagates. R_c should therefore depend on the microstructure.

Ponson et al. [86] analyzed the roughness of *i*-AlPdMn fracture surfaces. The scaling properties resemble those of various disordered materials.

The height-height correlation function reveals a self-affine behavior from the atomic scale up to $\xi \approx 2$nm. The Hurst exponent H is close to 0.72 (see Fig. 2 in Ponson et al. [86]). As the self-affine region includes the radius of the clusters $r_c \approx 0.5$nm, the authors state that the morphology of the fracture surfaces does not reflect the cluster distribution. Therefore, an influence of the clusters on physical properties is questioned.

The dispute whether or not the clusters should influence the height-height correlation function Δh[1] can be enlightened with the help of numerical experiments. Thus, the experimental findings at room temperature are compared to the results from atomistic simulations. The experimental surface data has been obtained by scanning tunneling microscopy. The molecular dynamics simulations have been performed in a representative icosahedral binary model quasicrystal at low temperature and load (see section 4.1.1). The fracture surfaces are geometrically scanned (see figure 3.3). The length scale of the model is given by r_0, the shortest distance between two X atoms (see chapter 1 and figure 1.1). Thus, the icosahedral system, the temperature as well as the contrast of the scanning images do not agree with the experimental situation. The experimental surfaces further may suffer from e.g. noise, anisotropy due to imaging, misorientation, signal amplification, and local geometric filtering[100]. In spite of these difficulties and differences, qualitative aspects of the experiments are resembled well by the simulations (see section 4.1.1).

In figure A.1 experimental findings (open symbols, Fig. 2 in [86]) are shown together with simulated results (solid symbols: orientation 2_2, load $k = 1.3$). As the data sets differ due to e.g. the different scanning techniques, temperatures, and models, Δh_{sim} has to be scaled by a factor of 3 for the simulations to allow a direct comparison. This shift e.g. indirectly indicates that the experimental surface has a higher root-mean-square roughness than the one simulated at very controlled conditions at low temperature. The absolute value of Δh, however, is not relevant for the following considerations. The characteristics of the curves and ξ already allow to decide whether Δh can give valuable in-

---

[1] The height-height correlation function Δh is defined by $\Delta h(\Delta \mathbf{r}) = \left\langle [h(\mathbf{r}' + \mathbf{e_r}\Delta r) - h(\mathbf{r}')]^2 \right\rangle^{0.5}$. Angular brackets denote the average over all $\mathbf{r}'$.

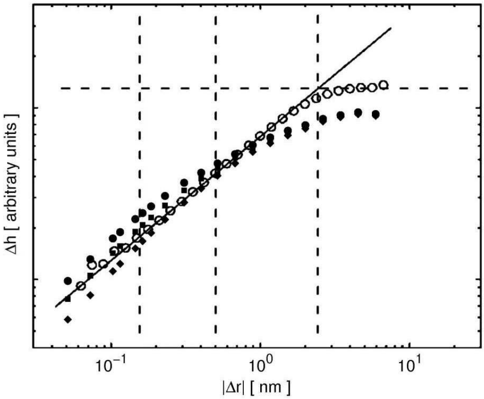

Figure A.1: Height-height correlation function Δh (open symbols: experiment, solid symbols: simulations). The size of an atom (discs), r_0 (squares), and $2r_0$ (diamonds) are used for the radius r of the scanning sphere. The atomic radius, the cluster radius, and ξ are indicated by vertical lines. The simulated results are scaled to allow a direct comparison of the characteristics of the curves.

formation on the role of the clusters.

Assuming that the crack front is propagating between indestructible spherical clusters, a drastic change in the behavior of Δh for $\Delta r \approx r_c$ could be expected. However, figure A.1 clearly shows that neither for the experiment nor for the simulations a hard crossover can be observed. However, Δh_{sim} is a bit more curved[2]. To investigate the influence of the scanning conditions on Δh, the radius r of the scanning sphere is varied (see figure A.1 and caption). Obviously, Δh depends on the tip size. Nevertheless, for the first few points on the left in figure A.1 all curves give $H \approx 0.7$. For the simulations, $\xi \approx 1\text{nm}$ is a reasonable assumption. Thus, as in the experimental findings, the self-affine region can include the radius of the clusters r_c. Detailed analyses of the simulated fracture surfaces prove that the clusters affect crack propagation in the model system (see section 4.1.1). So, in the simulations, the clusters play a crucial role despite $\xi \gtrsim r_c$. Consequently, one cannot conclude from $\xi > r_c$ that the clusters are not responsible for the morphology of the fracture surfaces. Moreover, Δh_{sim} shows a rather smooth behavior in figure A.1. Thus, even clusters that influence crack propagation do not necessarily lead to an *obvious* feature in the height-height correlation function. This is reasonable as the clusters are not unbreakable supermolecules. Without a sole relevant length scale, the lower limit of the power-law behavior is caused by the atomic size and not by the clusters. Furthermore, as shown by varying the tip size, details of the height-height correlation function may easily be hidden in experiments by limitations in the resolution of the scanning devices and any additional noise. In conclusion, a lack of a characteristic feature in the Δh curves does not allow to exclude an influence of the clusters on the fracture process.

---

[2] In this context, one has to note that the model system does not fully capture the self-similarity rules of icosahedral quasicrystals.

From this discussion it is evident that the results of Ponson et al. [86] cannot be used to disprove a physical role of the clusters. In contrary, the clusters help to understand the magnitude of ξ, which is related to the process zone size R_{c}. Icosahedral quasicrystals macroscopically behave elastically isotropic. However, locally, the response can change due to the clusters and the glue atoms in-between. If the clusters should directly affect crack propagation, their local deformation close to the crack tip should deviate from the linear elastic prediction. By definition, such a deviation only is possible *within* the process zone. Thus, the cluster scale should give an estimate for the size of the process zone. So, the relation $R_c \gtrsim r_c$ observed in experiment and simulation can be seen as a direct consequence of the physical role of the clusters in quasicrystals.

List of Figures

1.1 Icosahedral binary model 15
1.2 Basic four-layer stacking unit of the Friauf-Laves phases 17
1.3 C15 Friauf-Laves phase 18

2.1 The three modes of crack loading 19
2.2 Energy required for crack propagation 22
2.3 Orientations of slip planes 23

3.1 Simulation set-up 34
3.2 Visualization of fracture surfaces 36
3.3 Scanning of fracture surfaces 36

4.1 Lennard-Jones pair potentials 40
4.2 Fracture surfaces of the model quasicrystal 42
4.3 Cluster centers and surface energy 44
4.4 Clusters cut by a crack 44
4.5 Simulation and experiment 45
4.6 $111_{2\bar{1}\bar{1}}$ crack (model Friauf-Laves phase) 47
4.7 Atomic configurations (model Friauf-Laves phase) 48
4.8 010_{101} fracture surfaces (model Friauf-Laves phase) . . . 48
4.9 Comparison: quasicrystal vs. Friauf-Laves phase 49
4.10 Force-matched EAM potential functions 51
4.11 Analytical EAM potential functions 52
4.12 Stress-strain diagram 54
4.13 Surface energies (e-EAM) 58
4.14 Surface energies (fm-EAM) 58
4.15 Relaxation of a (111) surface 60
4.16 Comparison: $111_{2\bar{1}\bar{1}}$ cracks 61
4.17 Stacking sequences (e-EAM) 62
4.18 Orientations of the samples 64
4.19 Crack-tip position vs. time (010_{101}) 66
4.20 Crack-tip position vs. time (011_{100}) 66
4.21 Crack-tip position vs. time ($111_{0\bar{1}1}$) 67
4.22 Crack-tip position vs. time ($111_{2\bar{1}\bar{1}}$) 67
4.23 Crack velocities 68
4.24 Lower 010_{101} fracture surfaces 71
4.25 Upper 010_{101} fracture surfaces 72

4.26 Lower 011_{100} fracture surfaces 73
4.27 Upper 011_{100} fracture surfaces 74
4.28 Lower $111_{0\bar{1}1}$ fracture surfaces 75
4.29 Upper $111_{0\bar{1}1}$ fracture surfaces 76
4.30 Lower $111_{2\bar{1}\bar{1}}$ fracture surfaces 77
4.31 Upper $111_{2\bar{1}\bar{1}}$ fracture surfaces 78
4.32 Peak-to-valley roughness 79
4.33 Root-mean-square roughness 79
4.34 GLOK relaxator 81
4.35 Shifted seed cracks 81
4.36 $111_{2\bar{1}\bar{1}}$ crack 82
4.37 Crack-tip position vs. time ($111_{2\bar{1}\bar{1}}$ shifted) 82
4.38 Surface energies 83
4.39 Local energy cost for cleavage 85

A.1 Height-height correlation function 91

List of Tables

4.1 C15 $NbCr_2$ (collected data) 56
4.2 Surface energies (MD) 57
4.3 Ab-initio results (MBPP) 59

Bibliography

[1] F. F. Abraham, How fast can cracks move? A research adventure in materials failure using millions of atoms and big computers, *Adv. Phys.* **52** (2003) 727–790.

[2] F. F. Abraham, Unstable crack motion is predictable, *J. Mech. Phys. Solids* **53** (2005) 1071–1078.

[3] J. B. Adams and S. M. Foiles, Development of an embedded-atom potential for a bcc metal: Vanadium, *Phys. Rev. B* **41** (1990) 3316–3328.

[4] A. Al-Zu'bi, Theoretical study of structural defects related to fracture properties of intermetallic Laves phase compounds, *Master's thesis, Universität Stuttgart* (2005).

[5] H. L. Alberts, Elastic constants of a single crystal of Cr + 5 at.% V, *J. Phys. Cond. Mat.* **2** (1990) 9707–9711.

[6] M. P. Allen and D. J. Tildesley, *Computer Simulation of Liquids*, Oxford Science Publications, Clarendon Pr., Oxford (1987).

[7] H. C. Andersen, Molecular dynamics simulation at constant pressure and/or temperature, *J. Comput. Phys.* **72** (1979) 2384–2393.

[8] O. K. Andersen, Linear methods in band theory, *Phys. Rev. B* **12** (1975) 3060–3083.

[9] O. L. Anderson, A simplified method for calculating the Debye temperature from elastic constants, *J. Phys. Chem. Solids* **24** (1963) 909–917.

[10] Z. Bangwei, O. Yifang, L. Shuzhi, and J. Zhanpeng, An analytic MEAM model for all BCC transition metals, *Physica B* **262** (1999) 218–225.

[11] M. I. Baskes, J. S. Nelson, and A. F. Wright, Semiempirical modified embedded-atom potentials for silicon and germanium, *Phys. Rev. B* **40** (1989) 6085–6100.

[12] P. E. Blöchl, Projector augmented-wave method, *Phys. Rev. B* **50** (1994) 17953–17979.

[13] D. Bonamy, L. Ponson, S. Prades, E. Bouchaud, and C. Guillot, Scaling exponents for fracture surfaces in homogeneous glass and glassy ceramics, *Phys. Rev. Lett.* **97** (2006) 135504.

[14] M. Born and R. Oppenheimer, Zur Quantentheorie der Molekeln, *Ann. Phys. (Leipzig)* **389** (1927) 457–484.

[15] E. Bouchaud, Scaling properties of cracks, *J. Phys. Cond. Mat.* **9** (1997) 4319–4344.

[16] D. Broek, *Elementary engineering fracture mechanics*, Noordhoff International Publishing, Leyden (1974).

[17] P. Brommer, Entwicklung und Test von Wechselwirkungspotenzialen in Quasikristallen, *Diploma thesis* (2003) http://elib.uni–stuttgart.de/opus/volltexte/2003/1570/.

[18] P. Brommer and F. Gähler, Effective potentials for quasicrystals from ab-initio data, *Phil. Mag.* **86** (2006) 753–758.

[19] P. Brommer and F. Gähler, Potfit: effective potentials from ab-initio data, *Modelling Simul. Mater. Sci. Eng.* **15** (2007) 295–304, `http://www.itap.physik.uni-stuttgart.de/~imd/potfit/`.

[20] M. F. Chisholm, S. Kumar, and P. Hazzledine, Dislocations in complex materials, *Science* **307** (2005) 701–703.

[21] F. Chu, Y. He, D. J. Thoma, and T. E. Mitchell, Elastic constants of the C15 Laves phase compound $NbCr_2$, *Scripta Metall. Mater.* **33** (1995) 1295–1300.

[22] F. Chu, T. E. Mitchell, S. P. Chen, M. Sob, R. Siegl, and D. P. Pope, Experimental and theoretical studies on the C15 intermetallic compounds MV_2 (M=Zr, Hf and Ta): Elasticity and phase stability, *Mat. Res. Soc. Symp. Proc.* **364** (1995) 1389–1394.

[23] F. Chu, D. J. Thoma, Y. He, T. E. Mitchell, S. P. Chen, and J. H. Perepezki, Theoretical and experimental studies on the C15 intermetallic compound $NbCr_2$, *Mat. Res. Soc. Symp. Proc.* **364** (1995) 1089–1094.

[24] A. Corana, M. Marchesi, C. Martini, and S. Ridella, Minimizing Multimodal Functions of Continuous Variables with the “Simulated Annealing” Algorithm, *ACM Trans. Math. Soft.* **13** (1987) 262–280.

[25] M. S. Daw and M. I. Baskes, Semiempirical, Quantum Mechanical Calculation of Hydrogen Embrittlement in Metals, *Phys. Rev. Lett.* **50** (1983) 1285–1288.

[26] M. S. Daw, S. M. Foiles, and M. I. Baskes, The embedded-atom method: a review of theory and applications, *Mater. Sci. Rep.* **9** (1993) 251–310.

[27] J.-M. Dubois, Quasicrystals, *J. Phys. Cond. Mat.* **13** (2001) 7753–7762.

[28] M. Dzugutov, Glass Formation in a Simple Monatomic Liquid with Icosahedral Inherent Local Order, *Phys. Rev. A* **46** (1992) R2984 R2987.

[29] P. Ebert, M. Feuerbacher, N. Tamura, M. Wollgarten, and K. Urban, Evidence for a Cluster-Based Structure of AlPdMn Single Quasicrystals, *Phys. Rev. Lett.* **77** (1996) 3827–3830.

[30] P. Ebert, F. Yue, and K. Urban, Surface structures of cleaved icosahedral Al-Pd-Mn single quasicrystals after heat treatment, *Phys. Rev. B* **57** (1998) 2821–2825.

[31] C. Elsässer, N. Takeuchi, K. M. Ho, C. T. Chan, P. Braun, and M. Fähnle, Relativistic effects on ground state properties of 4d and 5d transition metals, *J. Phys. Cond. Mat.* **2** (1990) 4371–4394.

[32] V. Elser, Random tiling structure of icosahedral quasicrystals, *Phil. Mag. A.* **73** (1996) 641–656.

[33] F. Ercolessi and J. B. Adams, Interatomic potentials from first-principles calculations: the force-matching method., *Europhys. Lett.* **26** (1994) 583–588.

[34] E. Fawcett, Spin-density-wave antiferromagnetism in chromium, *Rev. Mod. Phys.* **60** (1988) 209–283.

[35] R. P. Feynman, Forces in Molecules, *Phys. Rev.* **56** (1939) 340–343.

[36] J. Fineberg and M. Marder, Instability in dynamic fracture, *Phys. Rep.* **313** (1999) 1–108.

[37] S. M. Foiles and J. B. Adams, Thermodynamic properties of fcc transition metals as calculated with the embedded-atom method, *Phys. Rev. B* **40** (1989) 5909–5915.

[38] J. B. Friauf, The crystal structure of Magnesium Di-Zincide, *Phys. Rev.* **29** (1927) 34–40.

[39] J. B. Friauf, The crystal structures of two intermetallic compounds, *J. Am. Chem. Soc.* **49** (1927) 3107–3114.

[40] A. A. Griffith, The phenomena of rupture and flow in solids, *Philos. Trans. R. Soc. London, Ser. A* **221** (1921) 163–198.

[41] P. Gumbsch, Brittle Fracture Processes Modelled on the Atomic Scale, *Z. Metallk.* **87** (1996) 341–348.

[42] P. Gumbsch, Modelling brittle and semi-brittle fracture processes, *Mater. Sci. Eng. A* **319-321** (2001) 1–7.

[43] P. Gumbsch and R. M. Cannon, Atomistic aspects of brittle fracture, *Mat. Research Society Bull.* **25** (2000) 15–20.

[44] P. Gumbsch, S. J. Zhou, and B. L. Holian, Molecular dynamics investigation of dynamic crack stability, *Phys. Rev. B* **55** (1997) 3445–3455.

[45] R. Haberlandt, S. Fritzsche, G. Peinel, and K. Heinzinger, *Molekulardynamik - Grundlagen und Anwendungen*, Friedrich Vieweg & Sohn Verlagsgesellschaft (1995).

[46] D. R. Hamann, M. Schlüter, and C. Chiang, Norm-Conserving Pseudopotentials, *Phys. Rev. Lett.* **43** (1979) 1494–1497.

[47] P. M. Hazzledine and P. Pirouz, Synchroshear transformations in Laves phases, *Scr. Mat. Metall.* **28** (1993) 1277–1282.

[48] C. L. Henley, Cell geometry for cluster-based quasicrystal models, *Phys. Rev. B* **43** (1991) 993–1020.

[49] C. L. Henley and V. Elser, Quasicrystal structure of (Al, Zn)$_{49}$Mg$_{32}$, *Phil. Mag. B* **53** (1986) L59 L66.

[50] K. M. Ho, C. Elsässer, C. T. Chan, and M. Fähnle, First-principles pseudopotential calculations for hydrogen in 4d transition metals: I. Mixed-basis method for total energies and forces, *J. Phys. Cond. Mat.* **4** (1992) 5189–5206.

[51] P. Hohenberg and W. Kohn, Inhomogeneous Electron Gas, *Phys. Rev.* **136** (1964) B864 B871.

[52] B. L. Holian and R. Ravelo, Fracture simulations using large-scale molecular dynamics, *Phys. Rev. B* **51** (1995) 11275–11288.

[53] S. Hong and C. L. Fu, Phase stability and elastic moduli of Cr$_2$Nb by first-principles calculations, *Interm.* **7** (1999) 5–9.

[54] W. G. Hoover, Canonical dynamics: Equilibrium phase–space distributions, *Phys. Rev. A* **31** (1985) 1695–1697.

[55] W. G. Hoover, A. J. C. Ladd, and B. Moran, High-Strain-Rate Plastic Flow Studied via Nonequilibrium Molecular Dynamics, *Phys. Rev. Lett.* **48** (1982) 1818–1820.

[56] G. R. Irwin, in *Encyclopedia of physics* (Edited by S. Flügge), volume VI: Elasticity and plasticity, pages 551–590, Springer-Verlag (1958).

[57] C. Janot, *Quasicrystals: A Primer*, Clarendon Press, Oxford (1994).

[58] C. Janot, Atomic clusters, local isomorphism, and recurrently localized states in quasicrystals, *J. Phys. Cond. Mat.* **9** (1997) 1493–1508.

[59] C. Janot and M. de Boissieu, Quasicrystals as a hierarchy of clusters, *Phys. Rev. Lett.* **72** (1994) 1674–1677.

[60] M. V. Jarić, *Introduction to Quasicrystals*, Academic Press, Incorporated (1988).

[61] H.-C. Jeong and P. J. Steinhardt, Cluster Approach for Quasicrystals, *Phys. Rev. Lett.* **73** (1994) 1943–1946.

[62] Z. H. Jin, P. Gumbsch, K. Lu, and E. Ma, Melting Mechanisms at the Limit of Superheating, *Phys. Rev. Lett.* **87** (2001) 055703.

[63] R. O. Jones and O. Gunnarsson, The density functional formalism, its applications and prospects, *Rev. Mod. Phys.* **61** (1989) 689–746.

[64] A. Kelly, W. R. Tyson, and A. H. Cottrell, Ductile and brittle crystals, *Phil. Mag.* **15** (1967) 567–586.

[65] J. Kohanoff and N. I. Gidopoulos, Density Functional Theory: Basics, New Trends and Applications, in *Handbook of Molecular Physics and Quantum Chemistry* (Edited by S. Wilson), volume 2, J. Wiley & Sons, Ltd. (2003).

[66] W. Kohn, Nobel Lecture: Electronic structure of matter – wave functions and density functionals, *Rev. Mod. Phys.* **71** (1999) 1253–1266.

[67] W. Kohn and L. J. Sham, Self-Consistent Equations Including Exchange and Correlation Effects, *Phys. Rev.* **140** (1965) A1133 A1138.

[68] G. Kresse and J. Furthmüller, Efficiency of ab-initio total energy calculations for metals and semiconductors using a plane-wave basis set, *Comp. Mat. Sci.* **6** (1996) 15–50.

[69] G. Kresse and D. Joubert, From ultrasoft pseudopotentials to the projector augmented-wave method, *Phys. Rev. B* **59** (1999) 1758–1775.

[70] S. K. Kwon, Z. Nabi, K. Kádas, L. Vitos, J. Kollár, B. Johansson, and R. Ahuja, Surface energy and stress release by layer relaxation, *Phys. Rev. B* **72** (2005) 235423.

[71] F. Laves and H. Witte, Die Kristallstruktur des $MgNi_2$ und seine Beziehungen zu den Typen $MgCu_2$ und $MgZn_2$, *Metallwirtsch.* **14** (1935) 645–649.

[72] F. Laves and H. Witte, Der Einfluß von Valenzelektronen auf die Kristallstruktur ternärer Magnesiumlegierungen, *Metallwirtsch.* **15** (1936) 840–842.

[73] D. Levine and P. J. Steinhardt, Quasicrystals. I. Definition and Structure, *Phys. Rev. B* **34** (1986) 596–616.

[74] M. Levy, Electron densities in search of Hamiltonians, *Phys. Rev. A* **26** (1982) 1200–1208.

[75] C. Li, B. Wang, and R. Wang, First-principles study of the effects of alloying elements (Al, Ni, Fe, Co) on the fracture behaviors of Cr_2Nb, *Conference contribution, The Eighth International Conference on Fundamentals of Fracture (ICFF VIII)* (3.-7.1.2008).

[76] J. D. Livingston, Laves-phase superalloys?, *Phys. Stat. Sol. A* **131** (1992) 415–423.

[77] S. G. Louie, K.-M. Ho, and M. L. Cohen, Self-consistent mixed-basis approach to the electronic structure of solids, *Phys. Rev. B* **19** (1979) 1774–1782.

[78] M. Marder, Molecular Dynamics of cracks, *Comp. Sc. Eng.* **1** (1999) 48–55.

[79] B. Mayer, H. Anton, E. Bott, M. Methfessel, J. Sticht, J. Harris, and P. C. Schmidt, Ab-initio calculation of the elastic constants and thermal expansion coefficients of Laves phases, *Interm.* **11** (2003) 23–32.

[80] H. J. Monkhorst and J. D. Pack, Special points for Brillouin-zone integrations, *Phys. Rev. B* **13** (1976) 5188–5192.

[81] J. R. Morris, C. Z. Wang, K. M. Ho, and C. T. Chan, Melting line of aluminum from simulations of coexisting phases, *Phys. Rev. B* **49** (1994) 3109–3115.

[82] N. F. Mott, Fracture of metals: Theoretical considerations., *Engineering* **165** (1948) 16–18.

[83] S. Nosé, in *Computer Simulation in Materials Science* (Edited by M. Meyer and V. Pontikis), pages 21–41, Kluwer Academic Publishers (1991), Computer Simulation in Materials Science.

[84] A. Ormeci, F. Chu, J. M. Wills, T. E. Mitchell, R. C. Albers, D. J. Thoma, and S. P. Chen, Total-energy study of electronic structure and mechanical behavior of C15 Laves phase compounds: $NbCr_2$ and HfV_2, *Phys. Rev. B* **54** (1996) 12753–12762.

[85] M. C. Payne, M. P. Teter, D. C. Allen, T. A. Arias, and J. D. Joannopoulos, Iterative minimization techniques for *ab initio* total-energy calculations: molecular dynamics and conjugate gradients, *Rev. Mod. Phys.* **64** (1992) 1045–1097.

[86] L. Ponson, D. Bonamy, and L. Barbier, Cleaved surface of *i*-AlPdMn quasicrystals: Influence of the local temperature elevation at the crack tip on the fracture surface roughness, *Phys. Rev. B* **74** (2006) 184205.

[87] M. J. D. Powell, A method for minimizing a sum of squares of non-linear functions without calculating derivatives, *Comp. J.* **7** (1965) 303–307.

[88] B. Quentrec, New Method for Searching of Neighbors in Molecular Dynamics Computations, *J. Comput. Phys.* **13** (1973) 430–432.

[89] J. R. Rice, Dislocation nucleation from a crack tip: an analysis based on the Peierls concept, *J. Mech. Phys. Solids* **40** (1992) 239–271.

[90] J. R. Rice and R. Thomson, Ductile versus brittle behaviour of crystals, *Phil. Mag. A* **73** (1974) 73–97.

[91] F. Rösch, Numerische Studien zur Rissausbreitung in dreidimensionalen komplexen Kristallstrukturen, *Diploma thesis* (2003) http://elib.uni–stuttgart.de/opus/volltexte/2004/1899/.

[92] F. Rösch, C. Rudhart, J. Roth, H.-R. Trebin, and P. Gumbsch, Dynamic fracture of icosahedral model quasicrystals: A molecular dynamics study, *Phys. Rev. B* **72** (2005) 014128.

[93] F. Rösch and H.-R. Trebin, Comment on "Cleaved surface of *i*-AlPdMn quasicrystals: Influence of the local temperature elevation at the crack tip on the fracture surface roughness", submitted to *Phys. Rev. B* (2008).

[94] F. Rösch, H.-R. Trebin, and P. Gumbsch, Fracture of complex metallic alloys: An atomistic study of model systems, *Phil. Mag.* **86** (2006) 1015–1020.

[95] F. Rösch, H.-R. Trebin, and P. Gumbsch, Interatomic potentials and the simulation of fracture: C15 $NbCr_2$, *Int. J. Fracture* **139** (2006) 517–526.

[96] J. Roth, Comment on 'Formation of a Dodecagonal Quasicrystal Phase in a Simple Monatomic Liquid', *Phys. Rev. Lett.* **79** (1997) 4042.

[97] J. Roth, Shock waves in complex binary solids: Cubic Laves crystals, quasicrystals, and amorphous solids, *Phys. Rev. B* **71** (2005) 064102.

[98] J. W. Roth, R. Schilling, and H.-R. Trebin, Nucleation of quasicrystals by rapid cooling of a binary melt: A molecular-dynamics study, *Phys. Rev. B* **51** (1995) 15833–15840.

[99] G. Schaaf, J. Roth, and H.-R. Trebin, Dislocation motion in icosahedral quasicrystals at elevated temperatures: numerical simulation, *Phil. Mag. A* **83** (2003) 2449–2465.

[100] J. Schmittbuhl, J.-P. Vilotte, and S. Roux, Reliability of self-affine measurements, *Phys. Rev. E* **51** (1995) 131–147.

[101] J. E. S. Socolar and P. J. Steinhardt, Quasicrystals. II. Unit-cell configurations, *Phys. Rev. B* **34** (1986) 617–647.

[102] J. Stadler, R. Mikulla, and H.-R. Trebin, IMD: a software package for molecular dynamics studies on parallel computers, *Int. J. Mod. Phys. C* **8** (1997) 1131–1140, `http://www.itap.physik.uni-stuttgart.de/~imd/`.

[103] P. J. Steinhardt, H. C. Jeong, K. Saitoh, M. Tanaka, E. Abe, and A. P. Tsai, Experimental verification of the quasi-unit-cell model of quasicrystal structure, *Nature* **396** (1998) 55–57.

[104] A. N. Stroh, A theory of the fracture of metals, *Advances in Physics* **6** (1957) 418–465.

[105] D. J. Thoma and J. H. Perepezko, An experimental evaluation of the phase relationships and solubilities in the Nb-Cr system, *Mater. Sci. Eng. A* **156** (1992) 97–108.

[106] R. Thomson, Physics of fracture, *Solid State Physics* **39** (1986) 1–129.

[107] R. Thomson, C. Hsieh, and V. Rana, Lattice trapping of fracture cracks, *J. Appl. Phys.* **42** (1971) 3154–3160.

[108] H.-R. Trebin, editor, *Quasicrystals. Structure and Physical Properties*, WILEY-VCH (2003).

[109] K. Urban and M. Feuerbacher, Structurally complex alloy phases, *J. Non-Cryst. Solids* **334 & 335** (2004) 143–150.

[110] D. Vanderbilt, Soft self-consistent pseudopotentials in a generalized eigenvalue formalism, *Phys. Rev. B* **41** (1990) 7892–7895.

[111] L. Vitos, A. V. Ruban, H. L. Skriver, and J. Kollár, The surface energy of metals, *Surf. Sci.* **411** (1998) 186–202.

[112] U. von Barth and C. D. Gelatt, Validity of the frozen-core approximation and pseudopotential theory for cohesive energy calculations, *Phys. Rev. B* **21** (1980) 2222–2228.

[113] A. von Keitz and G. Sauthoff, Laves phases for high temperatures — part II: Stability and mechanical properties, *Interm.* **10** (2002) 497–510.

[114] J. H. Wernick, in *Intermetallic Compounds* (Edited by J. H. Westbrook), pages 197–216, Wiley Series on the Science and Technology of Materials, John Wiley & Sons, Incorporated (1967).

[115] Q. B. Yang and K. H. Kuo, A new description of pentagonal Frank-Kasper phases and a possible structure model of the icosahedral quasicrystal, *Acta Crystallogr. Sect. A* **43** (1987) 787–795.

[116] O. Yifang, Z. Bangwei, L. Shuzhi, and J. Zhanpeng, A simple analytical EAM model for bcc metals including Cr and its application, *Z. Phys. B* **101** (1996) 161–168.

[117] E. H. Yoffe, The moving Griffith crack, *Phil. Mag.* **42** (1951) 739–750.

[118] S. J. Zhou, P. S. Lomdahl, R. Thomson, and B. L. Holian, Dynamic crack processes via molecular dynamics, *Phys. Rev. Lett.* **76** (1996) 2318–2321.

[119] IMD, the ITAP molecular dynamics program
(http://www.itap.physik.uni-stuttgart.de/∼imd/).

[120] MBPP, the ab-initio mixed-basis pseudopotential program (Max-Planck-Institut für Metallforschung, Stuttgart) B. Meyer, C. Elsässer, F. Lechermann, and M. Fähnle.

[121] potfit - a force-matching program
(http://www.itap.physik.uni-stuttgart.de/∼imd/potfit/).

[122] VASP, the Vienna ab-initio simulation package
(http://cms.mpi.univie.ac.at/vasp/).

Lebenslauf

Frohmut Rösch geboren am 20. März 1973 in Heilbronn

Eltern:	Ekkehard Friedrich Rösch (†14. März 2008) und Lilly Käthe Rösch geb. Schmidt
1980 - 1984	Besuch der Rosenauschule Heilbronn
1984 - 1993	Besuch des Justinus-Kerner-Gymnasiums Heilbronn Abschluss: Allgemeine Hochschulreife
1993 - 2003	Studium an der Universität Stuttgart im Studiengang Physik (Diplom) Abschluss: Diplom Während dieser Zeit: Mehrjährige häusliche Pflegetätigkeit
seit Sept. 2003	Promotion bei Prof. Dr. Hans-Rainer Trebin Institut für Theoretische und Angewandte Physik der Universität Stuttgart

Danksagung

Ich möchte mich an dieser Stelle bei allen bedanken, die zum Gelingen dieser Arbeit beigetragen haben.

- Herrn Prof. Dr. Hans-Rainer Trebin danke ich für die freundliche Aufnahme an seinem Institut, sowie für die interessante Aufgabenstellung und die Unterstützung bei ihrer Bearbeitung.

- Herrn Prof. Dr. Siegfried Schmauder danke ich für die Übernahme des Mitberichtes und die damit verbundene Mühe.

- Herrn Prof. Dr. Peter Gumbsch und Herrn Prof. Dr. Christian Elsässer danke ich für die sehr gute Zusammenarbeit während unseres gemeinsamen DFG Projektes. Bei Herrn Ali Al-Zu'bi (Masterarbeit) und Frau Olena Vedmedenko (Diplomarbeit) bedanke ich mich für ergänzende und weiterführende ab-initio Rechnungen zu den Friauf-Laves Phasen.

- Dr. Christoph Rudhart war mein Betreuer während der Diplomarbeit. Von ihm habe ich einen hervorragenden Einblick in die Simulation der Rissausbreitung erhalten.

- Herr Dr. Peter Brommer hat das Programm potfit entwickelt, das in dieser Arbeit zur Erzeugung von interatomaren Wechselwirkungen eingesetzt wurde.

- Dr. Franz Gähler hat das Molekulardynamikprogramm IMD gewissenhaft betreut und aktualisiert.

- Herr Dr. Ulrich Koschella und Herr PD Dr. Johannes Roth haben als Systemadministratoren stets eine problemlose Arbeit an den Computern ermöglicht.

- Meinem Kollegen Dr. Michael Engel danke ich für viele interessante Gespräche und Diskussionen.

- Mein Dank gilt allen Mitarbeitern und dem Sekretariat des Institutes für Theoretische und Angewandte Physik für die angenehme Arbeitsatmosphäre.

- Meinen Eltern gebührt mein ganz besonderer Dank. Ihnen ist diese Arbeit gewidmet.

Diese Arbeit wurde von der Deutschen Forschungsgemeinschaft (TR 154/20-1 & TR 154/25-1) finanziell gefördert und vom European Network of Excellence CMA unterstützt.